On the Kapitza instability and the generation of capillary waves

Georg F. Dietze

On the Kapitza instability and the generation of capillary waves

GEORG F. DIETZE[1],†

[1]Laboratoire FAST, Univ. Paris-Sud, CNRS, Université Paris-Saclay, F-91405, Orsay, France

(Received 10 December 2015)

We revisit the classical problem of a liquid film falling along a vertical wall due to the action of gravity, i.e. the Kapitza paradigm (*Zhurn. Eksper. Teor. Fiz.*, vol. 18, 1948, pp. 3-28). The free-surface of such a flow is typically deformed into a train of solitary pulses that consists of large asymmetric wave humps preceded by small precursory ripples, designated as "capillary waves". We set out to answer four fundamental questions: *(i)* By what mechanism do the precursory ripples form? *(ii)* How can they travel at the same celerity as the large-amplitude main humps? *(iii)* Why are they designated as "capillary waves"? *(iv)* What determines their wavelength and number and why do they attenuate in space? Asymptotic expansion as well as direct numerical simulations and calculations with a low-dimensional integral boundary layer model have yielded the following conclusions: *(i)* Precursory ripples form due to an inertia-based mechanism at the foot of the leading front of the main humps, where the local free-surface curvature is large. *(ii)* The celerity of capillary waves is matched to that of the large humps due to the action of surface tension, which speeds-up the former and slows-down the latter. *(iii)* They are justly designated as "capillary waves", because their wavelength is systematically shorter than the visco-capillary cut-off wavelength of the Kapitza instability. Due to a nonlinear effect, namely that their celerity decreases with decreasing amplitude, they nonetheless attain/maintain a finite amplitude because of being continuously compressed by the pursuing large humps. *(iv)* The number and degree of compression of capillary waves is governed by the amplitude of the main wave humps as well as the Kapitza number. Large-amplitude main humps travel fast and strongly compress the capillary waves in order for these to speed-up sufficiently. Also, the more pronounced the first capillary wave becomes, the more (spatially attenuating) capillary waves are needed to allow a smooth transition to the back of the next main hump. These effects are amplified by decreasing the Kapitza number, whereby, at very small values, streamwise viscous diffusion increasingly attenuates the amplitude of the capillary waves.

Key words: interfacial flows (free-surface), thin films, capillary waves

1. Introduction

We consider a Newtonian viscous liquid film flowing down a vertical wall due to the action of gravity in a two-dimensional setting. As shown in figure 1 and famously in the seminal experiments of Kapitza (1948), the free-surface of such a film may deform into a train of solitary pulses, travelling at constant celerity (Pumir *et al.* 1983) and displaying a very distinct shape. This consists of a large-amplitude asymmetric main hump in the form of a tear, which is preceded by a number of small ripples, typically designated as

† Email address for correspondence: dietze@fast.u-psud.fr

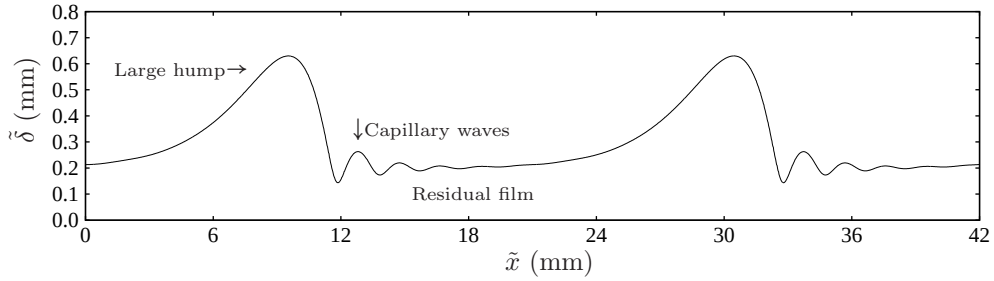

FIGURE 1. Fully-developed travelling free-surface profile of a vertically falling wavy liquid film: $Re{=}\tilde{q}/\nu{=}15$, $\tilde{f}{=}16$ Hz, $\Lambda{=}20.8$ mm, $Ka{=}\sigma/(\rho\, g^{1/3}\, \nu^{4/3}){=}509.5$. Large non-symmetric wave humps form due to the Kapitza instability (Kapitza 1948) and are preceded by so-called "capillary waves". How do these precursory waves form, how can they keep up with the large humps, why are they called "capillary waves", and what determines their wavelength and number?

"capillary waves", that form on the residual film separating subsequent wave trains. In this manuscript, we set out to answer a number of fundamental questions regarding this generic wave shape: *(i)* By what mechanism do the precursory ripples form? *(ii)* How can they travel at the same celerity as the large-amplitude main humps? *(iii)* Why are they designated as "capillary waves"? *(iv)* What determines their wavelength and number and why do they attenuate in space? First, we provide a short literature overview in order to put the objective of our manuscript into context.

Recent reviews on falling liquid films can be found in the monographs of Alekseenko *et al.* (1994), Chang & Demekhin (2002), and Kalliadasis *et al.* (2012) and the articles by Chang (1994) and Craster & Matar (2009). Early works elucidated the linear stability behaviour of this flow (Brooke Benjamin 1957; Yih 1963), showing the instability to be of the long-wave type at low Reynolds number values ($Re{=}\tilde{q}_0/\nu$, $\tilde{q}_0$ and ν designating the dimensional flow rate per unit width of the unperturbed film and kinematic viscosity, respectively), the stability cut-off being determined by surface tension, expressed through the Kapitza number ($Ka{=}\sigma/(\rho\, g^{1/3}\, \nu^{4/3})$, σ, ρ, and g denoting surface tension, density and gravity), and streamwise viscous diffusion (Ruyer-Quil & Manneville 1998). At large Re, short-wave shear modes were shown to occur (Floryan *et al.* 1987).

Later, numerical simulations based on the Navier-Stokes equations (Salamon *et al.* 1994; Ramaswamy *et al.* 1996; Miyara 1999; Malamataris *et al.* 2002; Gao *et al.* 2003; Nosoko & Miyara 2004; Trifonov 2008) and experiments using optical measuring techniques (Liu & Gollub 1994; Lel *et al.* 2005; Tihon *et al.* 2006; Dietze *et al.* 2009) focussed intensively on elucidating the kinematics of surface waves and the flow field they generate. This was complemented by the development of low-dimensional models (Benney 1966; Gjevik 1970; Shkadov 1967; Ruyer-Quil & Manneville 2000), which enable physically-consistent simulations on very long domains. Such simulations have represented the full transition of a wavy liquid film from its smooth-surface state at the inlet to interfacial spatio-temporal chaos several meters downstream (Chang *et al.* 1996). This evolution is associated with a number of secondary instabilities (Liu *et al.* 1993) as well as interaction and coalescence events between non-linear surface waves (Malamataris *et al.* 2002; Pradas *et al.* 2011). For brevity, we have focused here on two-dimensional studies and merely point out a number of works devoted to the more complicated three-dimensional problem (Joo & Davis 1992; Chang *et al.* 1993; Park & Nosoko 2003; Demekhin *et al.* 2007*a*,*b*, 2010; Kofman *et al.* 2014; Dietze *et al.* 2014).

In reviewing the above literature, we have found that questions *(i)* to *(iv)*, relating

to precursory capillary waves on falling liquid films, have, to the best of our knowledge, not been answered. Meanwhile, capillary waves play an important role for the dynamics of these wavy flows and a number of works have highlighted this point. For instance, Malamataris *et al.* (2002) have shown that capillary waves may prevent the coalescence of neighbouring large humps of moderately disparate amplitude and Pradas *et al.* (2013) discovered that self-sustained oscillations between large humps of same amplitude may occur when the latter are initially placed at a short distance from one another. Understanding how capillary waves form on wavy falling liquid films and under what circumstances they are most pronounced and greatest in number, may help to elucidate the mechanisms underlying such interactions.

On the other hand, capillary waves generate adverse pressure gradients sufficiently strong to overcome gravity and cause local flow reversal. This was, in principle, already conjectured by Kapitza (1948) based on his low-dimensional model and later confirmed by simulations based on the Navier-Stokes equations (Salamon *et al.* 1994; Miyara 1999; Malamataris *et al.* 2002), while the governing mechanism was elucidated by Dietze *et al.* (2008) and experimental proof was provided by Tihon *et al.* (2006) and Dietze *et al.* (2009). Meanwhile, Malamataris & Balakotaiah (2008) showed the existence of multiple flow reversal regions when several strongly-pronounced capillary waves are present and Dietze *et al.* (2014) identified regions of three-dimensional flow reversal. More recently, Doro & Aidun (2013), confirmed by direct numerical simulation (DNS) that flow reversal may also form for sinusoidal surface waves. The authors deduce from this that backflow "is not dependent on the presence of capillary waves." However, the wavelength of their sinusoidal waves is short and not very far from that of typical capillary ripples preceding the asymmetric large hump in figure 1. By understanding the nature of capillary waves on falling liquid films, our manuscript will help to establish whether it is necessary to distinguish these two wave types. Finally, a phase diagram for the onset of flow reversal was recently constructed by Rohlfs & Scheid (2015). Bearing in mind the controlling relevance of capillary waves for the onset of flow reversal, the current manuscript may help to provide a physical basis for such correlations.

In summary, despite a number of studies focussing on the effects of capillary waves on falling liquid films, the mechanisms governing their inception, growth, and final state as well as the matching of their celerity to that of the large humps, i.e. questions *(i)-(iv)*, seem not to have been understood yet. Nonetheless, a number of interesting indications toward answering these questions can be found in the literature. For instance, Ruyer-Quil & Manneville (2000), based on their WRIBL model, found that streamwise viscous diffusion plays an important role in shaping capillary waves. Also, two intriguing remarks were made by Chang (1994), who, referring to the wavelength of capillary waves, suggested "These humps have steep fronts which are relaxed by a series of front-running bow waves whose wavelength is close to the monochromatic waves at inception" and "the bow waves have a wave number close to the neutral wave number α_0 which is in excellent agreement with experimental observation." A fundamental question then is whether the wavelength of the "bow waves" is smaller or greater than the neutral stability cut-off, i.e. whether they are stable or unstable in terms of the primary Kapitza instability. In section 5, we provide an answer to this question. On a more general note, the wave profile in figure 1 is distinctly reminiscent of ripples forming around objects travelling on deep water. By elucidating the underlying mechanisms of capillary waves on falling liquid films, our manuscript will help judging if these two situations are indeed comparable.

The manuscript is structured as follows. In the first part, section 2, we discuss the mechanics of *single-peaked* surface waves occurring on an initially smooth falling liquid film due to the Kapitza instability. Such waves appear at low Re and can be described

with the so-called Benney equation (Benney 1966; Gjevik 1970), which we use to obtain analytic expressions for growth rate and celerity contributions resulting from different physical effects, linking the latter to the shape of the free-surface (through the film thickness δ and its derivatives). This part complements the qualitative description of the primary instability mechanism in Kalliadasis *et al.* (2012). It will serve in the second part of the manuscript, sections 3 to 5 devoted to the precursory capillary waves, which evolve from single-peaked solutions once the main hump amplitude becomes large. In part two, we use DNS of the Navier-Stokes equations, combined with the physical insight gained in the first part, to answer questions *(i)-(iii)* based on the flow conditions shown in figure 1 (which are outside the validity domain of the Benney equation). In the last part, section 6, we use the low-dimensional weighted residual integral boundary layer (WRIBL) model of Ruyer-Quil & Manneville (2000) to perform extensive parameter variations and answer question *(iv)*. In the conclusion, section 7, we summarize the principal results of the manuscript by succinctly answering the four questions we have posed at the onset. The appendix contains two figures showing additional simulation data, which will be relevant in section 3, and a third figure validating all employed simulation methods (based on the Benney, integral boundary layer, and Navier-Stokes equations, respectively) with experiments of Dietze *et al.* (2009). Also, the coefficients of the *second-order* Benney equation, which is used in section 2, are written out there.

2. Mechanics of single-peaked Kapitza waves

The occurrence of capillary waves on falling liquid films is inherently linked to conditions in the large humps that they precede. In fact, capillary waves evolve from single-peaked travelling wave solutions (consisting of a single hump and trough) once the amplitude of the main hump becomes large. Consequently, we start in this section by explaining the mechanics of single-peaked surface waves, developing on an initially smooth falling liquid film due to the Kapitza instability. In this limit, surface waves are of moderate amplitude and long length and can be described by asymptotic expansion (Oron *et al.* 1997) around the smooth film base flow, which results from an equilibrium between gravity and viscous stresses and is given by the dimensionless streamwise velocity profile:

$$u_0(y) = 3\left[y - \frac{y^2}{2}\right] \tag{2.1}$$

(y is the wall-normal or crosswise coordinate), where the length scale was chosen as the unperturbed film thickness $L{=}\tilde{\delta}_0{=}(3\,\tilde{q}_0\,(\mu/\rho)/g)^{1/3}$ (μ denotes dynamic viscosity and $\tilde{q}_0$ dimensional flow rate per unit width), and the velocity scale as the corresponding mean velocity $U{=}\tilde{q}_0/\tilde{\delta}_0$ (the time scale is L/U). Asymptotic expansion truncated at first order in the long-wave parameter $\epsilon{=}\tilde{\delta}_0/\Lambda$ (where Λ denotes the wavelength) yields the so-called Benney equation (Benney 1966; Gjevik 1970):

$$\partial_t\delta = -3\delta^2\,\partial_x\delta - \frac{3}{5}Re\left[12\,\delta^5\,(\partial_x\delta)^2 + 2\,\delta^6\,\partial_{xx}\delta\right] - \frac{1}{\mathrm{Bo}}\delta^2\left[3\,\partial_x\delta\partial_{xxx}\delta + \delta\partial_{xxxx}\delta\right], \tag{2.2}$$

written here in non-conservative form, which describes the evolution of the film thickness δ. On the RHS of (2.2), the first term expresses the balance between gravity and crosswise viscous diffusion, the second, scaled by the Reynolds number $Re = \tilde{q}_0\,\rho/\mu$, the effect of inertia, and the third, scaled by the inverse Bond number $\mathrm{Bo}{=}3/(Re\mathrm{We}){=}\rho\,g\,L^2/\sigma$ (where $\mathrm{We} = \sigma/(\rho\,U^2\,L)$ denotes the Weber number), the effect of surface tension σ.

In addition, by taking into account the integral continuity equation:

$$\partial_t\delta + \partial_x q = 0 \tag{2.3}$$

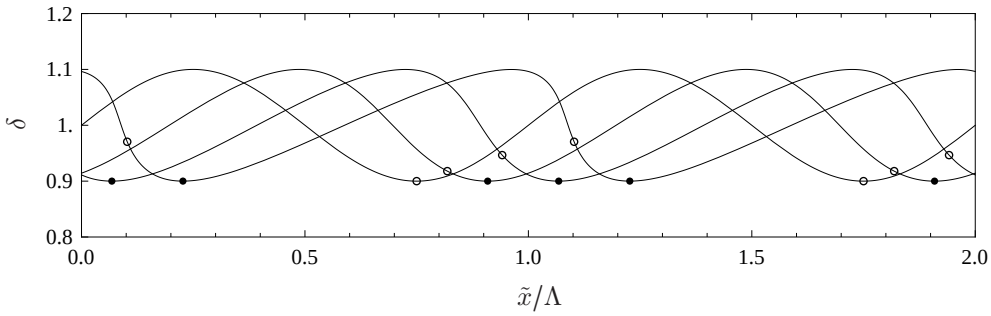

FIGURE 2. Kinematic wave governed by (2.7): $\tilde{\delta}_0$=0.1 mm, g=9.81 m/s^2, μ=0.001 Pas, ρ=1000 kg/m^3, Λ=100$\tilde{\delta}_0$. Starting from a harmonic initial condition, the wave moves from left to right at times $\tilde{t}$=0, 0.02, 0.04, and 0.06 s, steepening without growing in amplitude. Filled/open circles mark loci of minimal δ/maximal $\partial_{xx}\delta$ (at $\tilde{t}$=0, these points coincide).

(derived using the kinematic condition $v|_{y=\delta} = d\delta/dt$), a relation for the celerity of travelling waves ($d\delta$=0) can be obtained:

$$c = \partial_\delta q. \tag{2.4}$$

Employing the flow rate to film thickness relation underlying (2.2):

$$q = \delta^3\left[1 + \frac{6}{5}Re\,\delta^3\partial_x\delta + \frac{1}{\mathrm{Bo}}\,\partial_{xxx}\delta\right], \tag{2.5}$$

one then obtains from (2.4):

$$c = 3\delta^2 + \frac{36}{5}Re\,\delta^5\partial_x\delta + \frac{3}{\mathrm{Bo}}\,\delta^2\partial_{xxx}\delta + \frac{\Psi}{\partial_x\delta}, \tag{2.6a}$$

with

$$\Psi = \frac{6}{5}Re\,\delta^6\partial_{xx}\delta + \frac{1}{\mathrm{Bo}}\,\delta^3\partial_{xxxx}\delta. \tag{2.6b}$$

Equations (2.2) and (2.6a) will be used to highlight different mechanisms governing the growth rate and celerity of single-peaked waves. We will loosely refer to $\partial_t\delta$ as the "growth rate", although the proper form of a growth rate requires $\delta^{-1}\partial_t\delta$. Also, the local "growth rate" $\partial_t\delta$ is different from the total "growth rate" $d\delta/dt$=$\partial_t\delta + u|_\delta\,\partial_x\delta$, but the dynamics are contained in $\partial_t\delta$ and $\partial_t\delta$=$d\delta/dt$ at the wave extrema.

In the limit of inertialess flow without surface tension ($Re \to 0$, $1/\mathrm{Bo} \to 0$):

$$\partial_t\delta = -3\delta^2\,\partial_x\delta, \quad c = 3\delta^2, \quad q = \delta^3, \tag{2.7}$$

which describes so-called kinematic waves (Brooke Benjamin 1957) depicted in figure 2 for a representative set of parameter values. We may discern two key features from this (see Kalliadasis *et al.* (2012)): *(i)* The wave humps travel faster than the troughs ($c = 3\delta^2$), leading to a compression of the wave fronts and an elongation of the wave tails into a non-symmetric waveform. This development is never arrested, eventually leading to a shock (not shown in the graph); *(ii)* The growth rate at the extrema is zero and the wave amplitude imposed by the initial condition remains unchanged over time. From a physical point of view, kinematic waves occur because the flow rate q is greater in thicker than in thinner regions of the film, which, by mass conservation, drains regions of increasing and inflates regions of decreasing film thickness.

The cause for the growth of Kapitza waves is inertia. For this, we consider (2.2) and

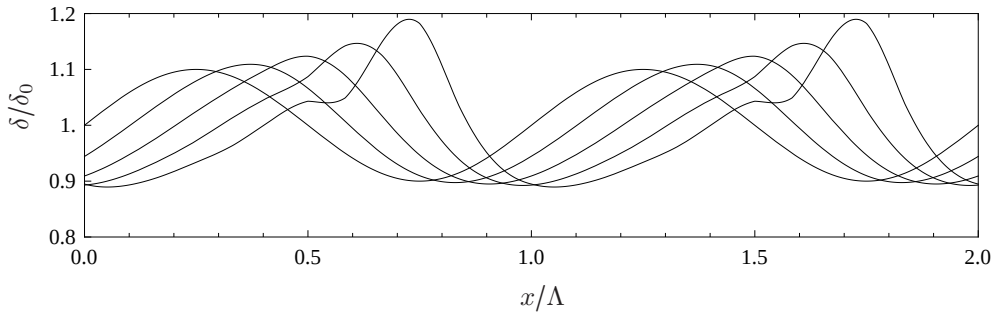

FIGURE 3. Dynamic wave governed by (2.8a): $\tilde{\delta}_0$=0.1 mm, g=9.81 m/s^2, μ=0.001 Pas, ρ=1000 kg/m^3, Λ=100 δ_0. Starting from a harmonic initial condition, the wave moves from left to right at times t=0, 0.01, 0.02, 0.03, and 0.04 s, growing in amplitude due to the effect of inertia.

(2.5) at *finite* Reynolds number and in the limit $1/\mathrm{Bo} \to 0$:

$$\partial_t \delta = -3\delta^2\,\partial_x\delta - \frac{3}{5}Re\left[12\,\delta^5\,(\partial_x\delta)^2 + 2\,\delta^6\,\partial_{xx}\delta\right], \tag{2.8a}$$

$$q = \delta^3\left[1 + \frac{6}{5}Re\,\delta^3\partial_x\delta\right]. \tag{2.8b}$$

Now the growth rate at the extrema is no longer null due to the second derivative $\partial_{xx}\delta$ in (2.8a). This causes wave humps, where $\partial_{xx}\delta < 0$, to grow in height and troughs, where $\partial_{xx}\delta > 0$, to grow in depth. The effect is scaled by δ^6 so that humps grow faster than troughs deepen. These features are illustrated in figure 3, plotting the solution of (2.8a) for the same parameters as figure 2. Because (2.8a) contains no attenuating terms, the amplitude of the waves in figure 3 eventually diverges, which is unphysical.

Mechanically, the effect of inertia can be explained as follows. Lack of it means that flow rate variations adapt infinitely fast to film thickness variations. In that case, considering two points either side of and infinitely close to an extremum, e.g. a wave crest, the associated film thicknesses are the same, and consequently, the flow rate in (2.7) does not vary. According to (2.3), the growth rate must thus be null. However, if inertia is present, the film thickness history, resulting from the passage of surface waves at the two points, must be taken into account. Indeed, the downstream point has just increased its film thickness (as $\partial_x\delta < 0$). Considering that the corresponding flow rate needs a finite time to react to this change, its value (2.8b) is thus slightly too low. Conversely, at the upstream point (where $\partial_x\delta < 0$), the flow rate is slightly too high. This leads to a negative $\partial_x q$ and thus a positive growth rate $\partial_t\delta$ at any wave hump. The contrary is true at a wave trough, where the free-surface curvature $\partial_{xx}\delta > 0$. Throughout this manuscript, we will refer to $\partial_{xx}\delta$ as the *free-surface curvature* although the precise formulation is $\partial_{xx}\delta/(1+\partial_x\delta)^{3/2}$. This is convenient and tenable, as the correction involving $\partial_x\delta$ vanishes at extrema, is negligible for long surface waves and does not influence the sign of the curvature. Meanwhile, the inertia-effect in (2.8) is scaled by powers of δ, because the flow rate adapts to film thickness variations by way of momentum diffusion in y-direction.

The second term in (2.8a), although it vanishes at the extrema, *does* play a role in the wave front and back, where it always (by being proportional to $(\partial_x\delta)^2$) decreases the growth rate. This again results from the inertia-induced lag (relative to the kinematic waves) of the flow rate in adapting to a time-varying film thickness and, in particular, the increase of lag magnitude with increasing film thickness. In the wave front, $\partial_x\delta < 0$ and the flow rate lag is decreasingly negative as δ decreases, causing a negative growth

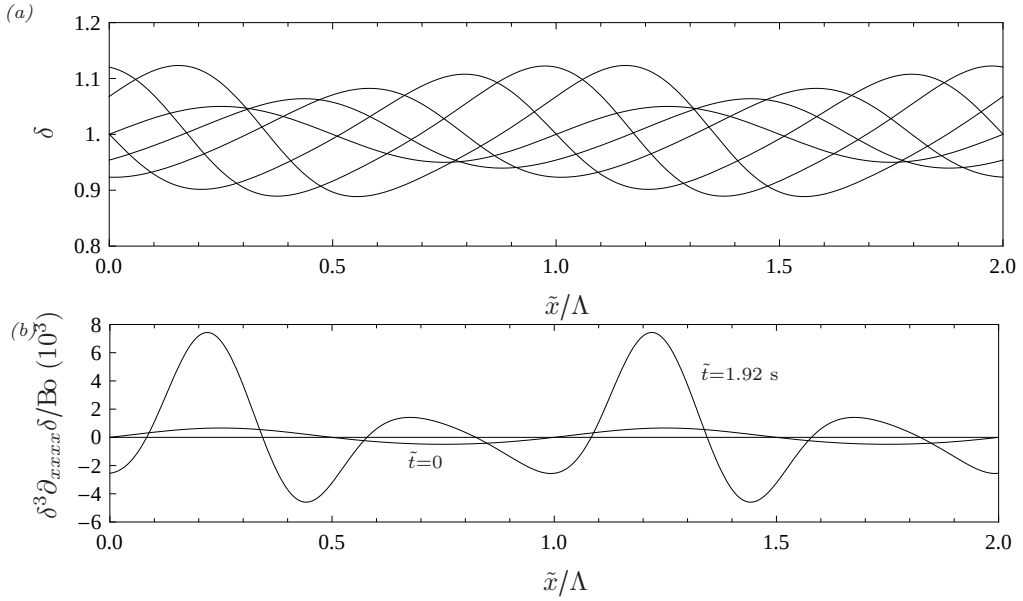

FIGURE 4. Saturating wave governed by (2.2): $\tilde{\delta}_0$=0.1 mm, g=9.81 m/s^2, μ=0.001 Pas, ρ=1000 kg/m^3, σ=0.072 N/m, Λ=100 $\tilde{\delta}_0$, Re=3.27. Starting from a harmonic initial condition, the wave moves from left to right at times $\tilde{t}$=0, 0.22, 0.54, 1.07, 1.8 and 1.92 s, growing initially and saturating to a constant amplitude due to the effect of surface tension forces. *(a)* Film thickness profile; *(b)* profile of $\delta^3\partial_{xxxx}\delta$/Bo in (2.2) evaluated at $\tilde{t}$=0 s, 1.92 s.

rate contribution: $\partial_x q > 0 \rightarrow \partial_t \delta < 0$. In the wave back, $\partial_x \delta > 0$ but the flow rate lag there is positive and increases with δ so that once again: $\partial_x q > 0 \rightarrow \partial_t \delta < 0$.

The saturation of Kapitza waves to a finite amplitude is caused by surface tension forces and their effect on the streamwise pressure gradient. For this, we consider the full form of equation (2.2), the solution of which is shown in panel 4a for the same parameters as in figures 2 and 3, additionally setting the surface tension to the value of water σ=0.072 N/m. This surface tension evidently causes the wave amplitude to saturate, creating a travelling wave of fixed shape in its own reference frame. The arrest of growth at the extrema is caused by the last term in (2.2) and determined by the sign of the fourth derivative $\partial_{xxxx}\delta$. Panel 4b plots this term for the initial (sinusoidal) profile and that of the final travelling wave. We see that $\partial_{xxxx}\delta$ is always negative at the troughs, increasing $\partial_t \delta$ according to (2.2), and positive at the humps, decreasing $\partial_t \delta$ there.

Physically, this can be explained by considering that $\partial_{xxx}\delta$ imposes the streamwise pressure gradient $\partial_x p = -\mathrm{We}\,\partial_{xxx}\delta$ through the effect of surface tension forces. Indeed, when moving from a wave trough toward a hump, the free-surface curvature decreases ($\partial_{xxx}\delta$ <0) and surface tension forces create a pressure gradient directed from the hump to the trough, which in simple terms tends to equalize film thickness variations. To be more accurate, the effect of this pressure gradient on the flow rate (2.5) must be considered. A pressure gradient directed counter to the flow will tend to reduce q and vice-versa. Spatial flow rate variations (which through (2.3) impose the local growth rate) can thus be generated by a change in pressure gradient, i.e. $\partial_{xx} p = -\mathrm{We}\partial_{xxxx}\delta \neq 0$. This introduces the fourth film thickness derivative, which, even for a sinusoidal profile (figure 4b), is positive at the humps ($\partial_{xx} p < 0 \rightarrow \partial_x q > 0 \rightarrow \partial_t \delta < 0$) and negative at the troughs ($\partial_{xx} p > 0 \rightarrow \partial_x q < 0 \rightarrow \partial_t \delta > 0$). Meanwhile, the effect scales with δ^3 in (2.2), so that

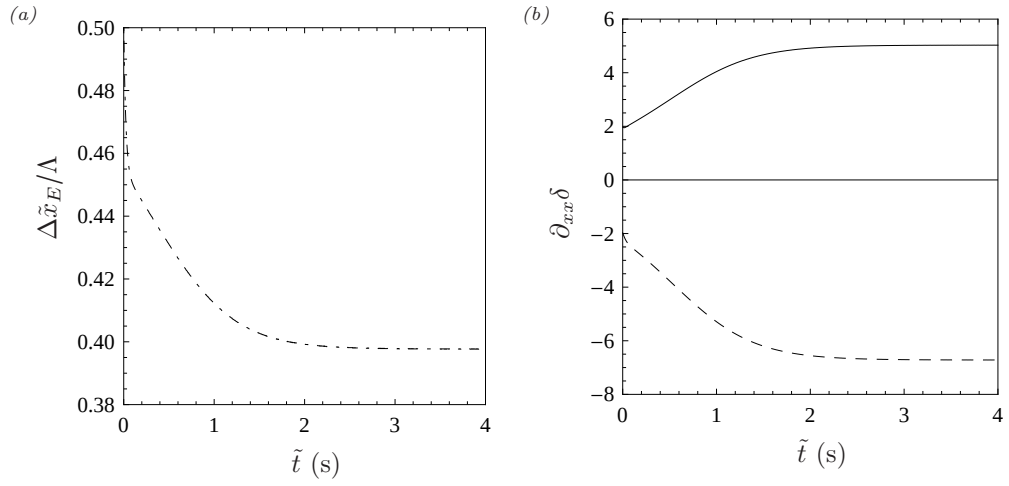

FIGURE 5. Free-surface evolution according to (2.2) as wave hump and trough converge in celerity. *(a)* Streamwise distance between trough and hump; *(b)* free-surface curvature at the hump (dashed line) and trough (solid line). Celerity matching is accompanied/generated by a streamwise compression of the hump-trough separation, increasing the curvature magnitudes.

it is stronger (and increasingly so with increasing δ) at the humps than at the troughs, nicely balancing the inertia-induced growth disparity between extrema. Physically, this scaling results from the sensitivity of the flow rate (2.5) to the pressure gradient, which accelerates/decelerates the flow over the entire film thickness.

In preparation of the second part of the manuscript, we seek to identify what mechanisms allow the trough and hump of the travelling wave in figure 4a to eventually propagate at the same celerity. The local celerity is given by (2.6*a*). At the extrema $x{=}x_E$, both $\partial_x\delta$ and Ψ tend to zero ($\lim_{x\to x_E}(\Psi){=}0$ follows from requiring a finite celerity), so that l'Hôpital's rule needs to be applied to the last term in (2.6*a*):

$$\Xi = \lim_{x\to x_E} \frac{\Psi}{\partial_x\delta} = \frac{6}{5} Re\, \delta^6 \frac{\partial_{xxx}\delta}{\partial_{xx}\delta} + \frac{1}{\mathrm{Bo}}\, \delta^3 \frac{\partial_{xxxxx}\delta}{\partial_{xx}\delta}, \tag{2.9a}$$

which yields:

$$c|_{x=x_E} = 3\delta^2 + \frac{3}{\mathrm{Bo}}\, \delta^2 \partial_{xxx}\delta + \Xi. \tag{2.9b}$$

Evaluating this relation for the profile at $t{=}1.92$ s in figure 4a, led to the following observations. The first term of (2.9*b*) is proportional to δ^2 and causes the wave hump to travel faster than the wave trough. This effect is amplified by the inertial term in (2.9*a*) because $\partial_{xxx}\delta < 0$ and the free-surface curvature is negative at the hump ($\partial_{xx}\delta < 0$) and positive at the trough ($\partial_{xx}\delta > 0$). Conversely (because $\partial_{xxxxx}\delta > 0$), this change in curvature between hump and trough tends to slow down the former and speed up the latter through the *capillary term* in (2.9*a*). It is thus the effect of surface tension, through the last term in (2.9*a*), that arrests the celerity disparity between humps and troughs.

Figure 5 plots the time evolution of the streamwise separation between wave hump and trough from figure 4 as well as the free-surface curvature at these positions. The initial celerity difference between the extrema causes a compression of the wave front (decreasing Δx_E) that is at first rapid and subsequently slower and degressive as the celerities converge. In the process, the magnitude of the free-surface curvature increases, whereby $|\partial_{xx}\delta|$ attains a greater value at the trough than at the hump.

We conclude by discussing the effect of streamwise viscous diffusion, which we will later show to play a role in shaping capillary waves. This effect enters asymptotic expansion at higher order and we must consider the Benney equation truncated at ϵ^2 (Lin 1974):

$$\begin{aligned}\partial_t\delta = \partial_t\delta_{(2.2)} - \partial_x\Big[&D\left(\partial_x\delta\right)^2 + E\,\partial_{xx}\delta + F\,\partial_{xxxx}\delta + G\,\partial_x\delta\,\partial_{xxx}\delta \\ &+H\left(\partial_{xx}\delta\right)^2\delta + I\left(\partial_x\delta\right)^2\partial_{xx}\delta\Big],\end{aligned} \tag{2.10}$$

where the coefficients D to I are all functions of δ and are given in the appendix (8.1), whereas the underlying relation for the flow rate is:

$$\begin{aligned}q = q_{(2.5)} &+ D\left(\partial_x\delta\right)^2 + E\,\partial_{xx}\delta + F\,\partial_{xxxx}\delta + G\,\partial_x\delta\,\partial_{xxx}\delta \\ &+H\left(\partial_{xx}\delta\right)^2\delta + I\left(\partial_x\delta\right)^2\partial_{xx}\delta.\end{aligned} \tag{2.11}$$

The contributions related to streamwise viscous diffusion are:

$$\partial_t\delta_\mu = -\partial_x\left[7\delta^3\partial_x\delta^2 + 3\delta^4\partial_{xx}\delta\right] \quad \text{and} \quad q_\mu = 7\delta^3\partial_x\delta^2 + 3\delta^4\partial_{xx}\delta. \tag{2.12}$$

In the first equation, only the term $-3\delta^4\partial_{xxx}\delta$ is non-zero at the extrema and thus the growth rate there is prescribed by the third film thickness derivative $\partial_{xxx}\delta$. Physically, this can be understood as follows. At zeroth order, the local instantaneous velocity profile is $u = 3\delta y - (3/2)y^2$ and so $\partial_{xx}u \approx 3y\partial_{xx}\delta$. This means that, at a wave hump ($\partial_{xx}\delta < 0$), fluid elements are subjected to an upstream resulting streamwise viscous stress, while the contrary is true at a wave trough ($\partial_{xx}\delta > 0$). This effect tends to reduce the flow rate at the hump and increase it at the trough (2.12). The corresponding streamwise change in flow rate $\partial_x q$ is then given by the change in free-surface curvature, i.e. $\partial_{xxx}\delta$, which is negative at both the wave hump and trough. Consequently, streamwise viscous diffusion increases the growth rate at both extrema $\partial_t\delta_\mu = -\partial_x q_\mu > 0$. Of course, for the trough, $\partial_t\delta_\mu > 0$ means that it grows less deep. As opposed to surface tension, the effect of streamwise viscous diffusion is thus "non-symmetrical".

Finally, let us consider how this affects the celerity at the extrema. Differentiating (2.11) with respect to δ, considering the limit $x = x_E$, and retaining only terms related to streamwise viscous diffusion, yields:

$$c_\mu\big|_{x=x_E} = 26\,\delta^3\,\partial_{xx}\delta + 3\delta^4\,\frac{\partial_{xxxx}\delta}{\partial_{xx}\delta}. \tag{2.13}$$

It turns out that both terms on the RHS of (2.13) counteract the celerity difference between maxima and minima resulting from (2.7). Indeed, the first term is proportional to the free-surface curvature, which tends to slow down the hump ($\partial_{xx}\delta < 0$) and speed up the trough ($\partial_{xx}\delta > 0$). The second term needs to be evaluated numerically. A calculation based on (2.10) for the same parameters as in figure 4 showed that $\partial_{xxxx}\delta > 0$ at the hump and $\partial_{xxxx}\delta < 0$ at the trough, which tends to further counteract celerity differences.

3. How are capillary waves generated?

Capillary waves evolve from single-peaked wave solutions once the wave amplitude becomes large. This happens at greater Reynolds number values than considered up until now, when the solution of (2.2) diverges due to the strong non-linearities contained therein (Pumir *et al.* 1983). Consequently, we will base our analysis in sections 3-5 on DNS of the Navier-Stokes equations using the volume-of-fluid/continuum-surface-force code Gerris (Popinet 2009). Nonetheless, the basic relationships identified in section 2 between governing mechanisms of wave growth/celerity and free-surface kinematics

Case	μ (Pas)	ρ (kg/m^3)	σ (N/m)	$\tilde{f}^\infty$ (Hz)	Λ (mm)	$\bar{\tilde{\delta}}$ (μm)	Re^∞	Bo
1	$3.13 \cdot 10^{-3}$	1098.3	0.0484	16	20.80	302	15.0	0.026
2	$3.13 \cdot 10^{-3}$	1098.3	0.0484	20	21.25	298	10.7	0.020

TABLE 1. Parameters for the DNS in section 3. The Kapitza number $Ka{=}\sigma/(\rho\, g^{1/3}\, \nu^{4/3}){=}509.5$ for both cases and "∞" denotes the hydrodynamically developed state. See appendix for validation of the two simulations with experiments by Dietze *et al.* (2009).

will help in identifying plausible physical mechanisms surrounding the inception and dynamics of capillary waves, which we will subsequently verify with our DNS data.

DNS of two representative flow scenarios (table 1) have been performed. These two simulations, case 1 and case 2, have been validated in the appendix with appropriate experiments (Dietze *et al.* 2009; Dietze 2010). They were conducted on a domain of length Λ using a periodic boundary condition in streamwise direction and starting from a sinusoidal film thickness perturbation about a flat film:

$$\delta|_{t=0} = \bar{\delta}\,[1 + \epsilon \cos(2\pi\, \tilde{x}/\Lambda)], \tag{3.1}$$

where the mean film thickness $\bar{\delta}$ and the domain length Λ represent the actual control parameters, which fix the Reynolds number Re^∞ and wave frequency f^∞ of the developed state (denoted by "∞"). The perturbation amplitude $\epsilon{=}0.4$ and the initial streamwise velocity $u|_{t=0} = 3\ \delta|_{t=0}\, y - (3/2)y^2$. We point out that the use of periodic boundary conditions fixes the volume of the liquid film to a constant throughout the simulation. Thus, it is the Reynolds number $Re{=}(\rho/(\Lambda\,\mu))\int_0^\Lambda \int_0^{\tilde{\delta}} \tilde{u}\, d\tilde{y}\, d\tilde{x}$ and wave frequency that vary over time, starting from a value set by the initial conditions and converging toward the fully developed values Re^∞ and f^∞. Though DNS studies showing the time evolution of surface waves have been performed before (Malamataris *et al.* 2002; Dietze *et al.* 2008; Doro & Aidun 2013), these have not focussed on explaining the inception of capillary waves.

The inception of capillary waves is a direct consequence of the primary Kapitza instability discussed in section 2 and the non-symmetric surface waves it generates. This is shown for case 1 in figure 6, depicting free-surface profiles evolving over time during growth of a large wave hump (see figure 8 for later times). The earliest, i.e. bottommost, profile displays a large asymmetric wave hump preceded by a single wave trough. It is similar to those plotted in figure 4a as it exhibits a single maximum and a single minimum. This remains so over roughly the next five profiles while growth of the wave hump increasingly compresses/steepens the wave front. However, from the eighth profile onwards, a new local wave trough, which we will call "capillary trough", develops near the foot of the wave front and increases in depth as time goes on, eventually undercutting the erstwhile global wave trough. This is highlighted by the inset in figure 6, showing a blown-up view of the free-surface profile in finer time resolution.

The underlying mechanism can be inferred as a first approximation by going back to the growth rate expression (2.2) (see discussion surrounding (3.2) for confirmation with DNS), where we had established the importance of free-surface curvature $\partial_{xx}\delta$ in driving inertia-induced growth. According to this, we conjecture that the capillary trough develops within the wave front of the main hump due to large positive curvature and associated inertia-induced negative growth there. The locus of maximal $\partial_{xx}\delta$ is highlighted with an open circle for each profile in figure 6. Interestingly, in the early stages, it does not correspond to the global film thickness minimum (filled circles). Rather, the maximum of $\partial_{xx}\delta$ occurs near the foot of the wave front, close to where the capillary trough eventually develops (onwards from profile 8). Growth in depth of this local trough further increases the related free-surface curvature and thus amplifies itself, causing it to become the new

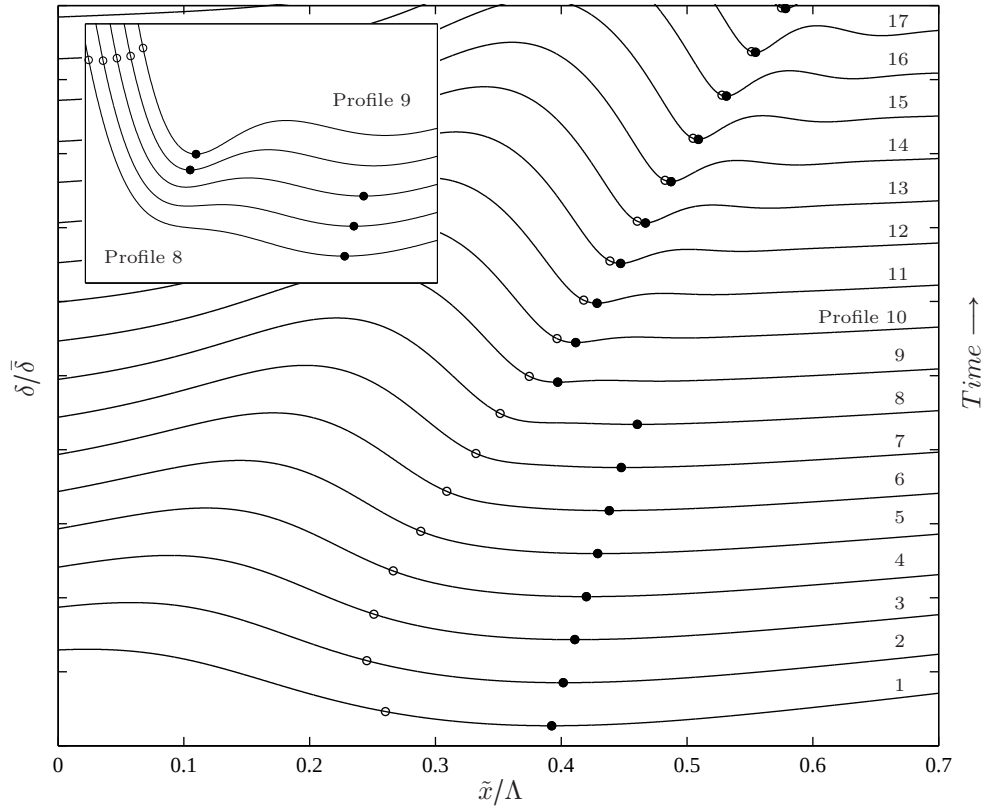

FIGURE 6. DNS of a vertically falling film: $\bar{\tilde{\delta}}$=302 μm, Re^{∞}=15, $\tilde{f}^{\infty}$=16 Hz, Ka=509.5 (see appendix for validation with experiments). Time evolution of the free-surface profile over the timespan $t = \tilde{t}/\tau \in [0.75 : 0.2 : 4.15]$ (time scale: $\tau=(H^3\rho/\sigma)^{1/2}$, with H=1.5 mm denoting the height of the DNS domain). Profiles in the main graph are represented over the film thickness interval $\delta/\bar{\delta} \in [0.4, 2.4]$ and those in the blown-up inset over $\delta/\bar{\delta} \in [0.6, 0.9]$. In the initial stages, as the main wave front steepens, a maximum of free-surface curvature (open circle) is established at its "foot" and not at the global wave trough (filled circle). According to (2.8*a*), this locally increases the magnitude of the (negative) growth rate there, eventually producing a new global film thickness minimum (see evolution between profiles 8 and 9 in inset), and, as a result, the first capillary wave, "sandwiched" between the former and actual global minimum.

global film thickness minimum from the ninth profile onwards. This self-amplification of the growth mechanism is demonstrated in figure 7, representing free-surface curvature profiles corresponding to the third to ninth (panel *a*) and the tenth (panel *b*) film thickness profiles in figure 6. Indeed, the curvature maximum therein (open circle) significantly increases during the development of the capillary trough (filled circle).

We point out that the capillary trough does not occur exactly at the free-surface curvature maximum, as can be seen in figures 6 and 7. This is because the curvature maximum appears within the wave front, where $\partial_x\delta < 0$ and the kinematic growth rate contribution (2.7) is positive (and dominates the slope-related inertial contribution in (2.8*a*)). Consequently, the total (negative) growth rate maximum is moved toward a position of lesser $|\partial_x\delta|$, i.e. slightly downstream. This kinematic retardation effect weakens with increasing Reynolds number (increasing relevance of inertia). We have verified this with an additional simulation that is almost identical to case 1, but starts from a greater

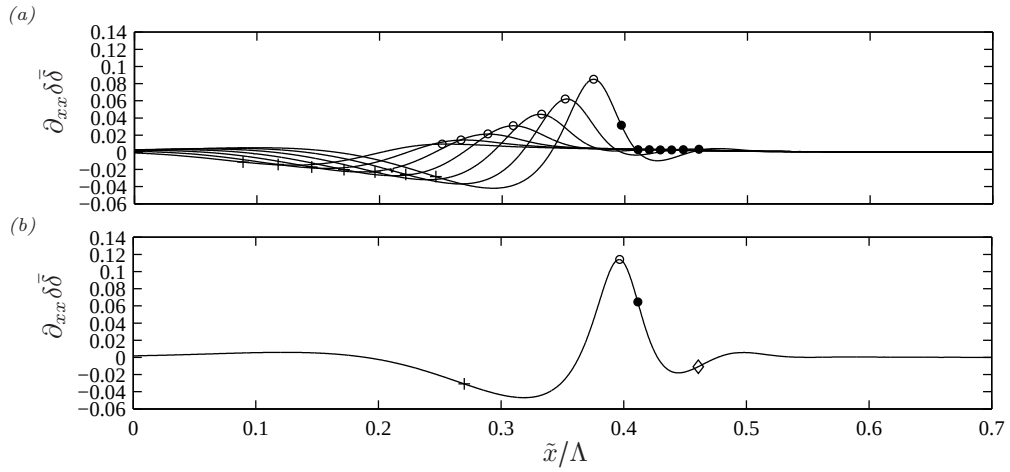

FIGURE 7. Profiles of the free-surface curvature $\partial_{xx}\delta$ corresponding to the third to ninth (panel a) and the tenth (panel b) profile in figure 6. The locus of the wave hump is marked with a plus sign, that of the wave trough with a filled circle, and that of the precursory capillary hump by a diamond (panel b), while the open circle marks the curvature maximum. Panel (a) shows that this curvature maximum occurs between the main hump and trough, causing the inertia-driven inception of a capillary trough at the foot of the wave front (figure 6). Because the depth of this trough increases, the associated curvature magnitude becomes very large (panel b).

initial Reynolds number value. Figure 20 in the appendix shows this simulation and may be directly compared to figure 6. For comparison, the instantaneous Reynolds number for the tenth profile is Re=13.5 in figure 6 while it is Re=38 in figure 20. Once the capillary trough has formed, $\partial_x\delta$=0 and the kinematic growth rate contribution vanishes.

Emergence of a capillary trough at the foot of the main wave front thus requires that the locus of the free-surface curvature maximum separates from that of the global wave trough. These loci coincide for the harmonic perturbation to which the film is initially subjected, and their separation is caused by the non-symmetric growth of the main hump. This ingredient is already contained in the kinematic waves plotted in figure 2, where open circles mark the curvature maximum and filled circles the film thickness minimum.

A consequence of the growing capillary wave trough in figure 6 is that it produces a local maximum of *negative* curvature slightly further downstream (figure 7), owing to the necessity to "reconnect" the free-surface to the predominantly flat film separating neighbouring large wave humps. This negative curvature generates the capillary *hump* seen to emerge from the tenth profile onwards in figure 6. Panel 7b, where the locus of the capillary hump is highlighted with a diamond, suggests that this is again caused by the curvature-related inertial growth mechanism. Because this mechanism is self-amplifying, the capillary hump, just as the capillary trough, quickly grows as time progresses (figure 6). Figure 8 shows this evolution at later times. Therein, we see that growth of the first capillary hump eventually generates a second capillary trough further downstream, which itself produces another capillary hump and so on and so forth. This series of capillary humps, "sandwiched" between capillary troughs, is what we call "capillary waves".

Given that the physical explanations presented above are based on equation (2.2), which, strictly-speaking, is not valid for wave regimes deviating substantially from the primary flow, we check them against the Navier-Stokes equations. We will show that the latter confirm the main physical mechanisms identified with (2.2). For this, we focus on two of the profiles in figures 6 and 8: *(i)* The eighth profile in figure 6 (t^* = 2.15) where

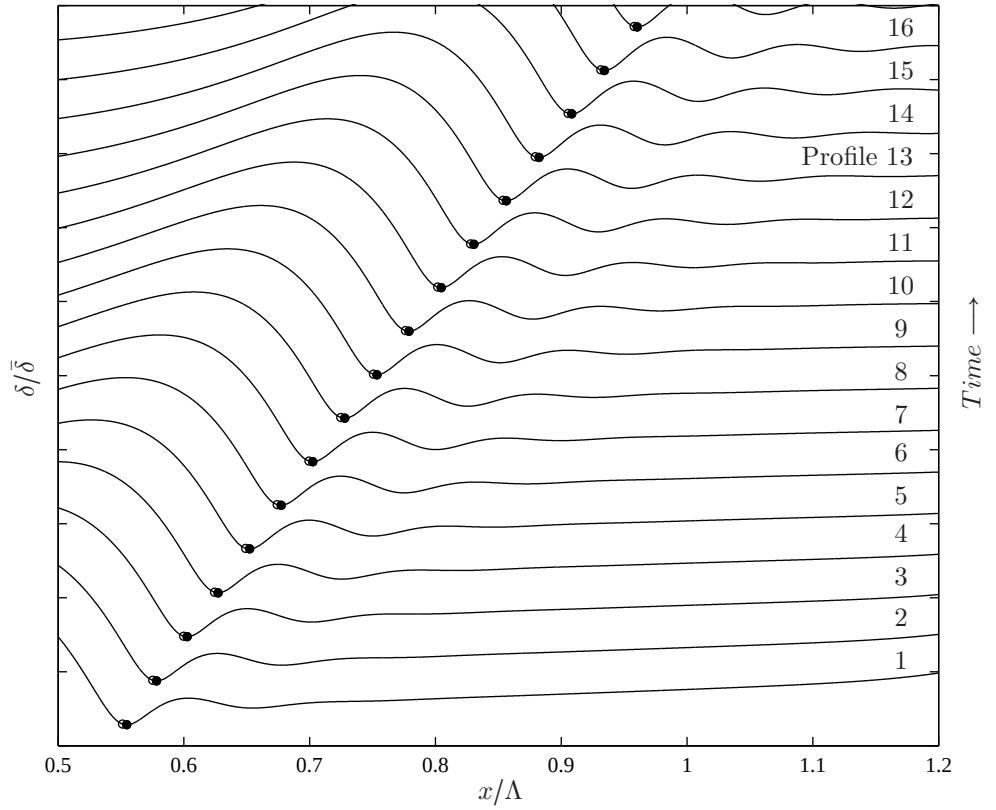

FIGURE 8. Capillary wave evolution following early events in figure 6. The timespan is $t^* = \tilde{t}/\tau \in [3.95 : 0.2 : 7.15]$ (time scale τ as in figure 6). Growth of the first capillary trough kicks-off the creation of additional capillary humps/troughs of decreasing curvature magnitude.

the capillary trough is just about to appear, and *(ii)* the thirteenth profile in figure 8 ($t^* = 6.55$) where the capillary waves are much closer to saturation.

To untangle the different mechanisms governing $\partial_t\delta$, we derive a similar expression to (2.2) based on the Navier-Stokes equations. This is done in three steps successively applied to the differential x-momentum balance. First, isolate $\partial_{yy}u$ (crosswise viscous diffusion term) and integrate in y direction twice to isolate the streamwise velocity $u(y)$ (using $u|_{y=0}$=0 and $\partial_y u|_{y=\delta}$=0 in the process). Second, integrate across the film thickness to isolate the flow rate $q = \int_0^\delta u(y)dy$:

$$q = \underbrace{Re\int_0^\delta\int_0^y\int_y^\delta -\frac{du}{dt}d^3y}_{T_i} + \underbrace{Re\int_0^\delta\int_0^y\int_y^\delta -\partial_x p d^3y}_{T_p} + \underbrace{3\int_0^\delta\int_0^y\int_y^\delta d^3y}_{T_g} + \underbrace{\int_0^\delta\int_0^y\int_y^\delta \partial_{xx}u d^3y}_{T_\mu}. \tag{3.2a}$$

Third, differentiate in streamwise direction to isolate $\partial_t\delta$=$-\partial_x q$:

$$\partial_t\delta = -\partial_x q = -\partial_x T_i - \partial_x T_p - \partial_x T_g - \partial_x T_\mu. \tag{3.2b}$$

This equation can be applied to the DNS data to quantify the growth rate contributions of inertia, pressure, gravity, and streamwise viscous diffusion (T_i, T_p, T_g, and T_μ). Figure 9 represents profiles of the dominant terms in (3.2*b*) (panels 9b and 9d) as well as the

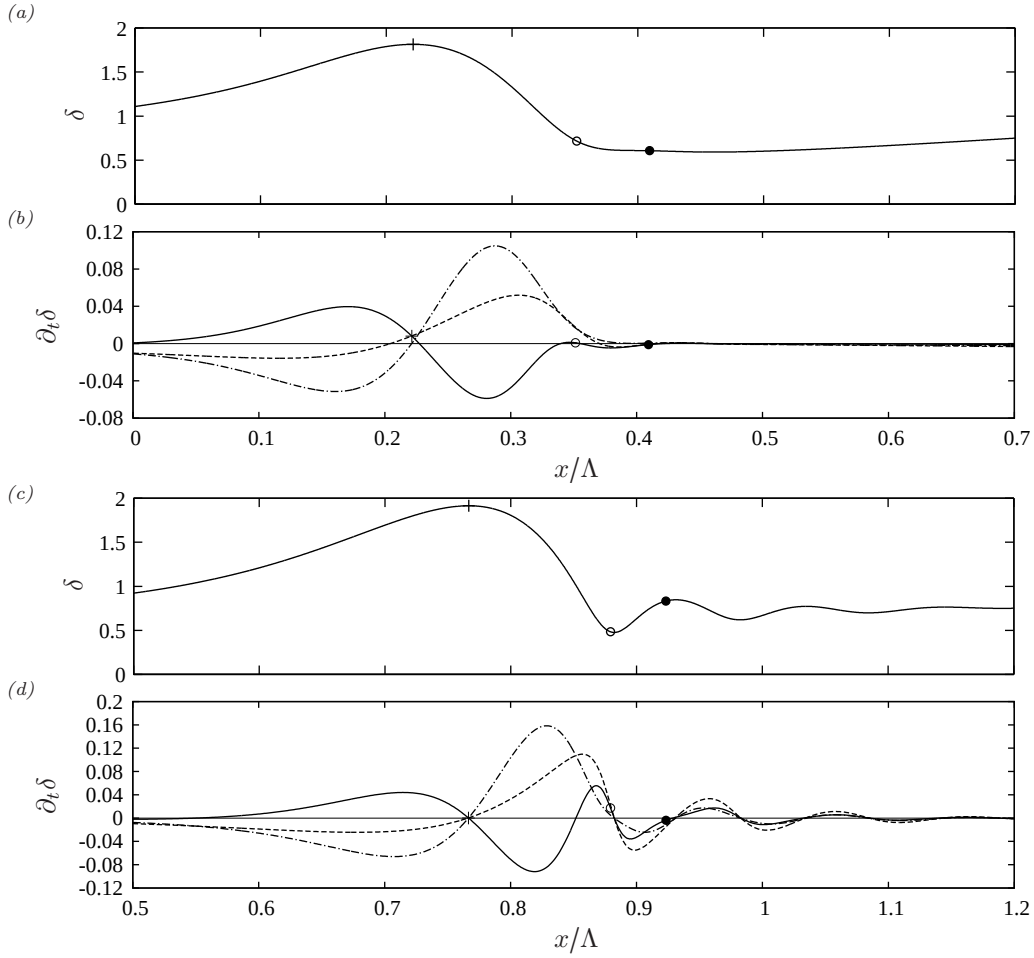

FIGURE 9. Different contributions to the growth rate $\partial_t\delta$ in the region of the capillary waves for two different time points. *(a,b)* Early stage (eighth profile in figure 6, $t^* = 2.15$); *(c,d)* Wave structure closer to saturation (thirteenth profile in figure 8, $t^* = 6.55$). Panels *(a,b)* depict film thickness profiles, and panels *(c,d)* profiles of different contributions to the growth rate according to (3.2*b*). Dashed lines: $\partial_t\delta$; dot-dashed lines: $-\partial_x T_g = -3\partial_x\delta$; solid lines: $-\partial_x\,(T_i + T_p + T_\mu)$; open circles: curvature maximum; filled circles: local curvature minimum.

corresponding free-surface profiles (panels 9a and 9c) at the two above-mentioned time points. Plus signs mark the locus of the main wave maximum, open circles that of the curvature maximum (roughly where the first capillary trough appears), and filled circles that of the adjacent local curvature minimum (roughly where the first capillary hump appears). Dashed lines in panels 9b and 9d represent the growth rate $\partial_t\delta$. The contribution of gravity, just as for kinematic waves (2.7), can be evaluated to $-\partial_x T_g = -3\partial_x\delta$ and is plotted with dot-dashed lines. It is null at extrema and cannot explain the growth nor decay of capillary humps and troughs. Rather, this growth is governed by a balance between the destabilizing effect of inertia $-\partial_x T_i$ and the stabilizing effects of capillary-induced pressure gradients $-\partial_x T_p$ and streamwise viscous diffusion $-\partial_x T_\mu$. Solid lines in panels 9b and 9d represent this balance, i.e. $-\partial_x(T_i + T_p + T_\mu)$.

Starting with the earlier time point (panels 9a and 9b), we see that the kinematic growth rate contribution (dot-dashed line in panel 9b) follows the gradient of the wave

profile, assuming negative values in the wave back, positive values in the wave front, and zero at the extrema. The growth rate $\partial_t\delta$ (dashed line) roughly follows this evolution with two exceptions: $\partial_t\delta$ is positive at the main wave hump (plus sign), which is thus growing, and negative at the position where the first capillary trough is about to appear (slightly downstream of the open circle). Inspecting the profile of $-\partial_x(T_i+T_p+T_\mu)$ (solid line in panel 9b), which is positive at the first and negative at the second position, we deduce that this growth follows from an excess in the destabilizing inertial contribution $-\partial_x T_i$. Our qualitative statements based on (2.2) are thus confirmed.

As the capillary waves approach saturation, we expect the stabilizing growth rate contributions -$\partial_x T_p$ and -$\partial_x T_\mu$ to play an increasing role. This is confirmed by panels 9c and 9d. Therein, we observe that $-\partial_x T_p$ and $-\partial_x T_\mu$ have taken the upper hand at both the capillary trough (open circle) and hump (filled circle), causing a slight reversal of growth rates there. Incidentally, these stabilizing contributions already play a role at the earlier time point (panel 9b) as they significantly counteract the inertial effect at the curvature maximum (open circle), which contributes to moving the point where the first capillary trough will appear slightly downstream.

Figure 10 shows the *time evolution* of the mechanisms at play during inception, growth, and attenuation of the first capillary trough and hump. It represents time traces of the film thickness (panel 10a), free-surface curvature (panel 10c), and growth rate $\partial_t\delta$ (panel 10d), as well as individual contributions $-\partial_x T_i$, $-\partial_x T_p$, and $+\partial_x T_\mu$ (panels 10e and 10f). Thereby, T_μ was approximated with $\partial_{xx}(q/\delta)\delta^3/3$ to avoid excessive error amplification when differentiating the numerical data. In addition, panel 10b depicts time traces of the streamwise separation Δx between main-hump/capillary-trough (plus signs), capillary-trough/capillary-hump (diamonds), and main-hump/capillary-hump (circles).

Panel 10a shows that the capillary trough (circles) increasingly deepens in the early stages, reaches a minimum, and then slowly approaches its saturated depth. The corresponding free-surface curvature (panel 10c) is correlated quite well with the depth of the trough but it is also affected by its width (panel 10b). Reciprocal observations apply to the first capillary hump (diamonds). In terms of the mechanisms underlying these kinematics, panel 10e confirms our prior assumption that the growth rate contribution of inertia $-\partial_x T_i$ (solid line) is destabilizing, while that of pressure $-\partial_x T_p$ (dot-dashed line) and streamwise viscous diffusion $-\partial_x T_\mu$ (dashed line) is stabilizing. Indeed, at the capillary trough, $-\partial_x T_i$ is negative while the other terms are positive (the opposite applies to the capillary hump, which is not shown here). We point out that $-\partial_x T_i$ and $-\partial_x T_p$ in the earliest stages are exceedingly small and could not be (individually) evaluated reliably due to numerical errors. These data were omitted from panel 10e.

Of course, the growth rate $\partial_t\delta$ is finally determined by a balance of the three effects. Although the inertial and pressure terms are far greater in magnitude than the viscous term, the latter still plays an important role as the former partially cancel each other. This is shown in panel 10f, which compares $-\partial_x T_i - \partial_x T_p$ to $+\partial_x T_\mu$ at the capillary trough (circles) and hump (diamonds), respectively (note that $+\partial_x T_\mu$ and not $-\partial_x T_\mu$ is plotted here to better compare magnitudes of same-symbol curves). We see that $-\partial_x T_i - \partial_x T_p$ and $-\partial_x T_\mu$ are comparable in magnitude, meaning that streamwise viscous diffusion significantly shapes capillary waves in falling liquid films. This is in-line with Ruyer-Quil & Manneville (2000), who showed that taking it into account in their model significantly damped the capillary waves (see figure 5 in that reference). The destabilizing effect of inertia $-\partial_x T_i$ by and large surmounts the stabilizing effect of pressure $-\partial_x T_p$, meaning that variations of $-\partial_x T_i - \partial_x T_p$ in magnitude (as compared to $-\partial_x T_\mu$) and not in sign dictate whether the capillary waves grow or decay. This is confirmed by the strong correlation between $\partial_t\delta$ (panel 10d) and $|-\partial_x T_i - \partial_x T_p|$ (panel 10f).

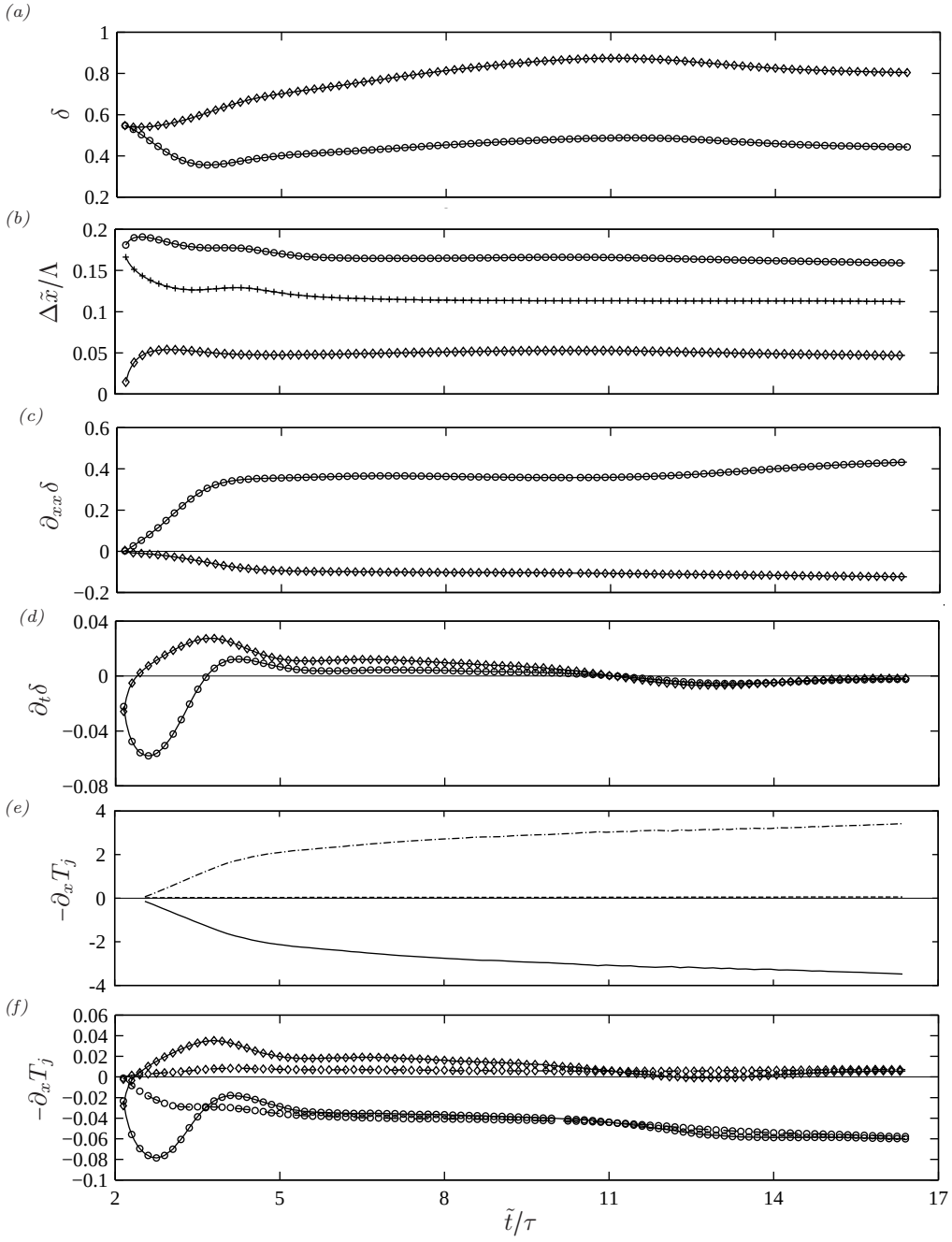

FIGURE 10. Dynamics of capillary ripples. Time traces at the first capillary trough (circles) and hump (diamonds). *(a,c,d)* Film thickness, free-surface curvature, and growth rate; *(b)* distance between main-hump/capillary-trough (plus signs), capillary-trough/capillary-hump (diamonds), and capillary-hump/main-hump (circles); *(e)* different growth rate contributions at the first capillary *trough* according to (3.2*b*): inertia $-\partial_x T_i$ (solid line), pressure $-\partial_x T_p$ (dot-dashed line), and streamwise viscous diffusion $-\partial_x T_\mu$ (dashed line); *(f)* comparison of $-\partial_x T_i - \partial_x T_p$ (solid line) and $+\partial_x T_\mu$ (dashed line). Inertia drives growth of the capillary trough and hump against the stabilizing effects of capillary-induced pressure gradients and streamwise viscous diffusion.

By comparing the mechanical contributions plotted in panels 10e and 10f with the kinematic quantities plotted in panels 10a to 10d, we may draw the following main conclusions. Inertia is indeed responsible for the inception and growth of the first capillary trough. This growth is arrested by capillary-induced pressure gradients and streamwise viscous diffusion once the local film thickness (panel 10a) and the width of the capillary trough (panel 10b) have become sufficiently small, while the local curvature (panel 10c) has become large. Indeed, increasingly compressing the deepening capillary trough between the main and capillary humps, creates large gradients of curvature (augmenting capillary-induced pressure gradients) and film thickness (augmenting streamwise velocity gradients and viscous stresses). Reciprocal observations apply to the first capillary hump, which saturates at a much smaller amplitude than the main hump because the short wavelength imposed by the capillary trough immediately produces large curvature gradients. The smaller capillary hump in turn produces a less pronounced second capillary trough and so on and so forth. Precursory capillary ripples, which are initiated in the most curved portion of the steepening front of a single-peaked wave hump, thus come to their saturation in the form of a compressed (and attenuating) capillary wave train, exhibiting large gradients in free-surface curvature and film thickness.

4. Celerity matching: How do capillary waves keep up?

In this section, we investigate through what mechanism capillary waves eventually adjust their celerity to that of the much greater main humps. Evaluating $c = \partial_x q/\partial_x \delta$ at extremal points using l'Hôpital's rule ($\partial_x \delta{=}0$ and, if c is assumed to be finite, $\partial_x q$ must also tend to zero), yields the celerity $c|_{x=x_E} = \partial_{xx} q/\partial_{xx}\delta|_{x=x_E}$ there, which may be decomposed into its respective dynamic contributions based on (3.2*a*):

$$c = \frac{\partial_{xx} q}{\partial_{xx}\delta} = \underbrace{\partial_{xx} T_i/\partial_{xx}\delta}_{c_i} + \underbrace{\partial_{xx} T_p/\partial_{xx}\delta}_{c_p} + \underbrace{\partial_{xx} T_g/\partial_{xx}\delta}_{c_g} + \underbrace{\partial_{xx} T_\mu/\partial_{xx}\delta}_{c_\mu}, \tag{4.1}$$

where the subscript $x = x_E$ was omitted for convenience. The contribution of gravity can be evaluated to $c_g = 3\delta^2$ and corresponds to the celerity of kinematic waves (2.7). Strictly speaking, (4.1) only holds for waves of constant amplitude, i.e. when $d\delta{=}0$, but we will nonetheless apply it to characterize conditions prior to saturation. This amounts to a quasi-stationary treatment of the celerity evolution.

The different celerity contributions in (4.1) are plotted in figure 11 (over the same timespan as figure 10) at the main hump (plus signs) and capillary trough (open circles), respectively, while figure 12 plots the corresponding film thickness, curvature and streamwise separation. Panels 11a and 11b show that the kinematic contribution c_g (symbol-only curves) tends to impose a much greater celerity at the main hump than at the capillary trough, owing to the considerable difference in film thickness between these locations. Nonetheless, the full celerity c (solid lines) at the two extrema is eventually matched at $c \approx 2.5$. In the process, the celerity of the main hump drops much more significantly with respect to c_g than that of the capillary trough rises. This is driven by the interplay between the contributions of capillary-induced pressure variations c_p and inertia c_i.

Separate evaluation of these contributions proved problematic due to amplification of numerical errors that withstood the good spatio-temporal resolution of our simulation (the time increment was $\Delta\tilde{t}{=}10^{-8}$ s and the minimal film thickness $\tilde{\delta}_{\min} \approx 150\,\mu$m was resolved with about 25 grid points). However, for the larger Re simulation in figure 20, the problem is lesser. We thus refer to figure 21 in the appendix, which plots separate time traces of c_p and c_i for that very similar simulation. These show that the celerity

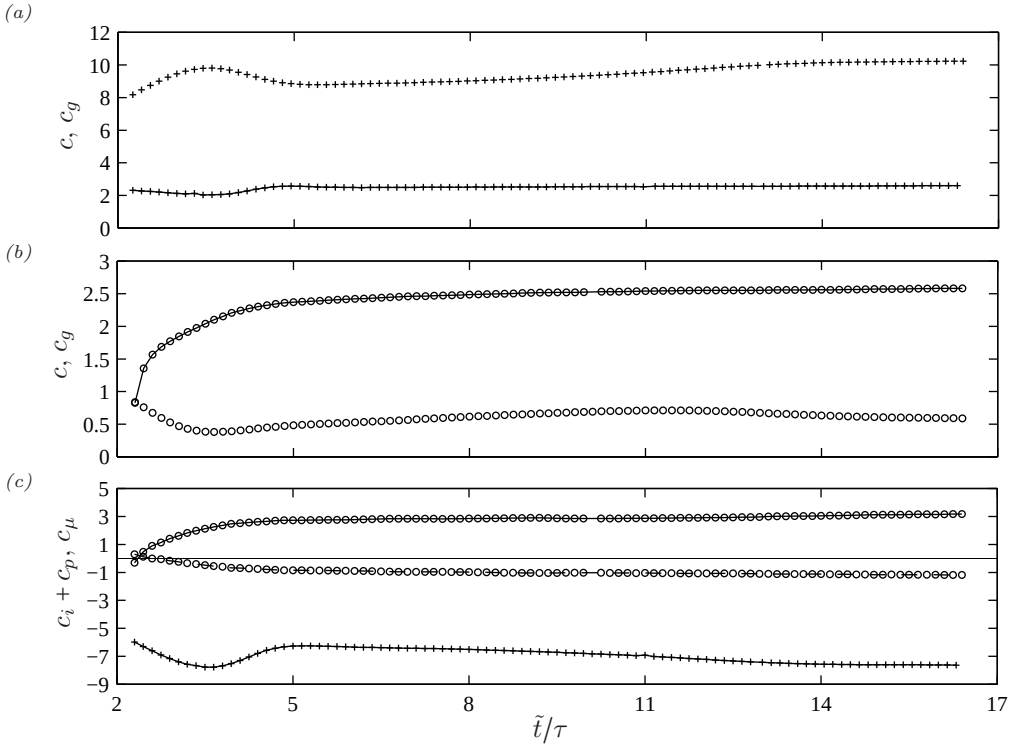

FIGURE 11. Time evolution (τ as in figure 8) of different contributions to the wave celerity according to (4.1) evaluated at the main hump (plus signs) and capillary trough (open circles). *(a,b)* Full celerity c (solid lines) and contribution of gravity c_g (symbols only); *(c)* resulting contribution of inertia and pressure $c_i + c_p$ (solid line) and contribution of streamwise viscous diffusion c_μ (dashed line). At the hump, c_μ is noisy but negligibly small and thus not shown.

of the capillary trough is increased by capillary-induced pressure gradients ($c_p > 0$, dot-dashed lines) and decreased by inertia ($c_i < 0$, solid lines), while the opposite holds at the main hump ($c_p < 0$, $c_i > 0$). The sum of the two celerity contributions $c_i + c_p$ is plotted in figure 11c (solid lines), showing that c_p dominates c_i, which increases the celerity of the capillary trough and decreases that of the main hump. Meanwhile, the contribution of streamwise viscous diffusion c_μ is considerable at the capillary trough (dashed line), decreasing its speed, and negligibly small at the hump (data not plotted).

Comparing solid lines in panels 11a and 11b, we see that the capillary trough initially travels much (two times) slower than the main hump and then speeds up significantly, while the main hump slows down only slightly. The acceleration of the capillary trough is driven by the streamwise separation between main hump and capillary trough/hump. Indeed, in the early stages, the fast-approaching main hump increasingly compresses the capillary trough (panel 12c), while increasing its curvature (panel 12b). This in turn causes $|c_p|$ to rise with respect to $|c_i|$ (panel 11c) and thus speeds up the capillary trough. We point out that similar mechanics govern the evolution of all subsequent capillary humps and troughs, until all celerities are matched and all amplitudes are saturated.

The main hump's celerity (panel 11a) and amplitude (panel 12a) are arrested when the leading wave front steepens (panel 12c) while coming up on the initially slow capillary trough, increasing $|\partial_{xx}\delta|$ at the wave maximum (panel 12b). In this sense, we may also conclude that capillary waves limit the celerity and amplitude of the main humps.

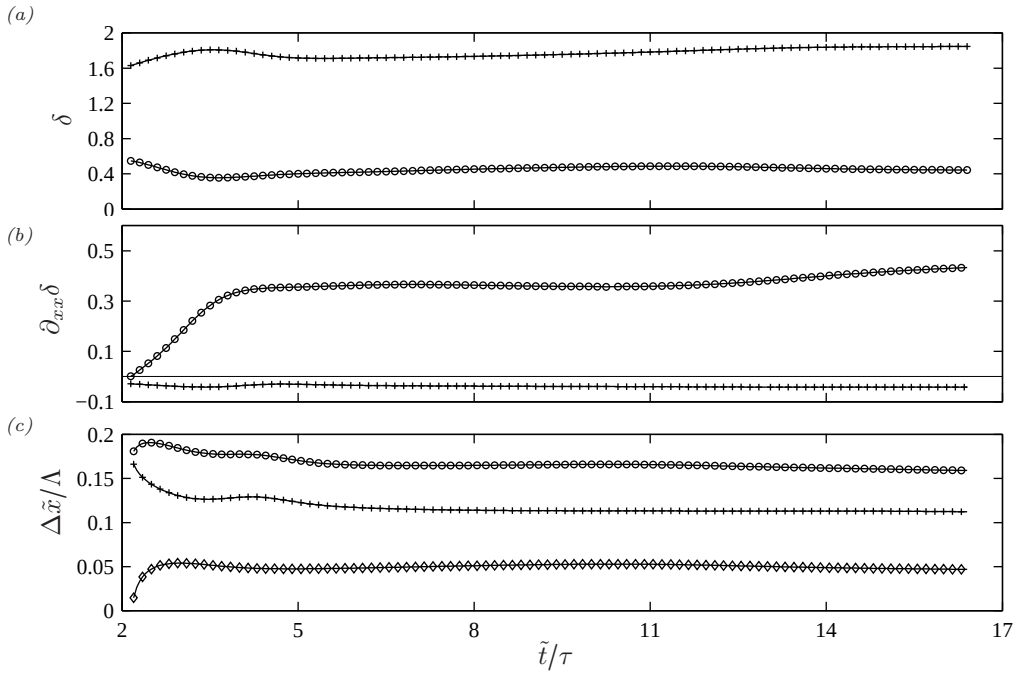

FIGURE 12. Evolution (τ as in figure 8) of the shape of the main hump (plus signs) and capillary trough (open circles) over the time span in figure 11. *(a)* Film thickness δ; *(b)* free-surface curvature $\partial_{xx}\delta$; *(c)* streamwise separation between main-hump/capillary-hump (open circles), main-hump/capillary-trough (plus signs), and capillary-trough/capillary-hump (diamonds).

In summary, celerity matching between main humps and capillary waves is achieved when these structures are compressed into a wave train of sufficiently large free-surface curvature magnitudes at the extrema, allowing capillary-induced pressure gradients c_p (and streamwise viscous diffusion c_μ) to slow down the main hump and speed up the capillary trough. We observed in section 2 that these mechanisms strongly scale with δ. Assuming this holds qualitatively in figure 12, it explains why $|\partial_{xx}\delta|$ at the capillary trough is much greater than at the main hump (panel 12c).

5. Why are they called "capillary waves"?

Throughout this manuscript, we have used the words "capillary waves" to designate the small ripples preceding the large wave humps in figure 1. However, we have not explained the capillary nature of these ripples. We have shown that their growth is arrested by surface tension forces (as well as streamwise viscous diffusion), but this is also true for the main wave humps. Something else must thus be at play.

It turns out that the wavelength of capillary waves on falling liquid films is systematically shorter than the visco-capillary cut-off wavelength of the Kapitza instability. Figure 13 shows this for a large variety of wave trains (see figures 17-19 for profiles) computed using the simplified second-order Weighted Residual Integral Boundary Layer (WRIBL) model of Ruyer-Quil & Manneville (2000), which has been validated against experiments and DNS in the appendix. This model, coupled with the continuation software Auto07P (Doedel 2008), allowed parameter sweeps at moderate computational cost. Solid lines in panels 13a-13d represent the dimensionless wave number of the first capillary wave

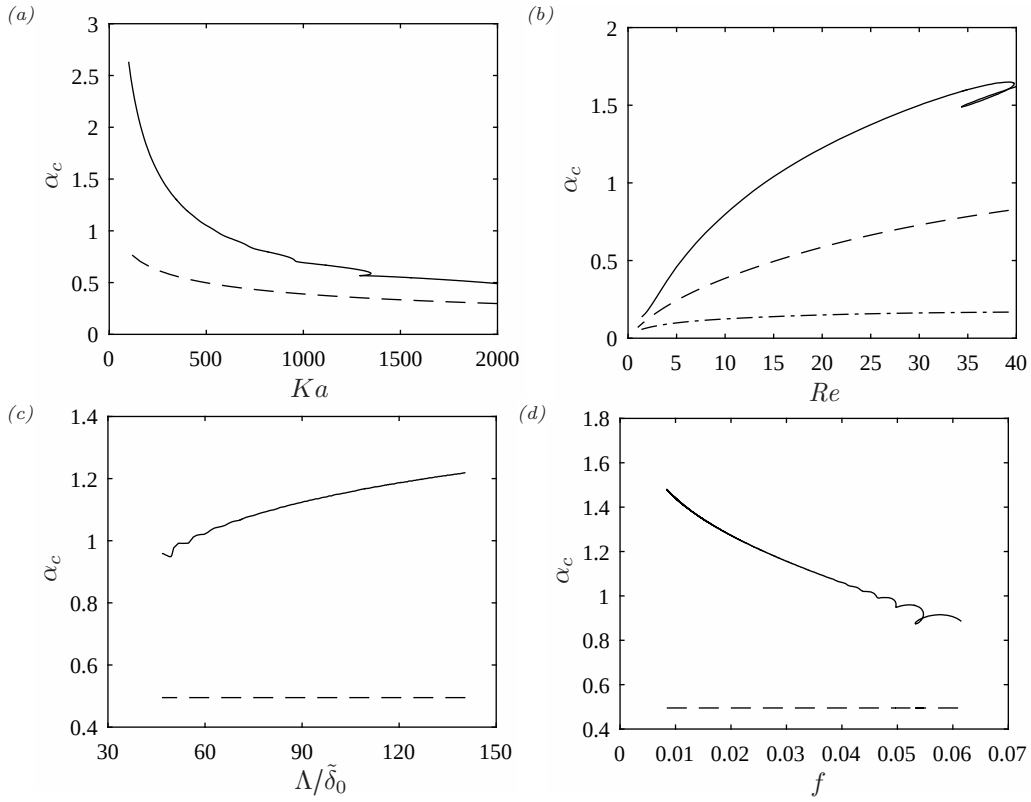

FIGURE 13. Wave number of first capillary wave $\alpha_c{=}2\pi\tilde{\delta}_0/\Lambda_c$ (solid lines) compared to visco–capillary cut-off of the Kapitza instability (dashed lines). Solid lines: simplified second order WRIBL model (Ruyer-Quil & Manneville 2000); dashed lines: Orr-Sommerfeld temporal linear stability analysis (Brooke Benjamin 1957). Parameters vary about case 1 in table 1: *(a)* influence of the Kapitza number $Ka{=}\sigma/(\rho\, g^{1/3}\,\nu^{4/3})$; *(b)* influence of the Reynolds number Re; *(c)* influence of the large hump wavelength Λ; *(d)* influence of the large hump frequency f. All quantities are non-dimensionalized with primary flow scales except for the dot-dashed line in panel *(b)* which rescales the dashed-line-data using $\tilde{\delta}_\nu{=}(\mu/\rho)^{2/3}g^{-1/3}{=}93.9$ μm. The wave number of capillary waves is systematically greater than the visco-capillary cut-off. Thus, these waves are stable in terms of the primary Kapitza instability and justly designated as "capillary waves".

$\alpha_c{=}2\pi\tilde{\delta}_0/\Lambda_c$, where Λ_c is the streamwise distance between the first and second capillary trough, as a function of the Kapitza number Ka, Reynolds number Re, wavelength Λ, and frequency f, respectively. We use the Kapitza number $Ka{=}\sigma/(\rho\, g^{1/3}\,\nu^{4/3})$ here instead of the Bond number because it contains only fluid properties.

Dashed lines in panels 13a-13d represent the visco-capillary cut-off wave number of the primary Kapitza instability, which was obtained by linear stability analysis of the Navier-Stokes equations (Brooke Benjamin 1957; Yih 1963). It is apparent in figure 14a, plotting linear temporal growth rate versus wave number for selected parameter combinations. The cut-off wave number is the short-wave intersection with the α-axis and decreases with decreasing Reynolds number/increasing Kapitza number. It is of visco-capillary nature because both surface tension and streamwise viscous diffusion (see figure 3 in Ruyer-Quil & Manneville (1998)) stabilize the inertia-driven Kapitza instability.

Comparing solid and dashed lines in figure 13, we may thus conclude: Capillary waves on falling liquid films are systematically shorter than the visco-capillary cut-off wave-

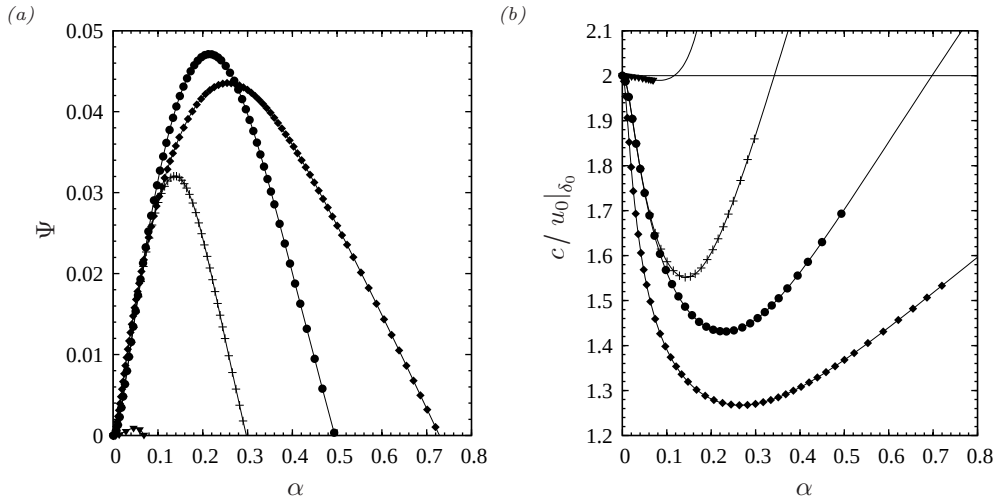

FIGURE 14. Temporal linear stability data obtained from Orr-Sommerfeld solution. *(a)* Growth rate Ψ (non-dimensionalized with $\tilde{\delta}_0/\,\tilde{u}_0|_{\tilde{\delta}_0}$) versus wave number; *(b)* celerity versus wave number. Parameters vary about case 1 (filled circles) in table 1. •: Re=15, Ka=509.5; ▾: Re=1, Ka=509.5; ◆: Re=30, Ka=509.5; +: Re=15, Ka=2000. The visco-capillary cut-off wave number (panel *a*) decreases with decreasing Reynolds number and increasing Kapitza number. Celerity–matched waves of increasingly disparate wave number are possible beyond the unstable branch (highlighted by symbols in panel *b*), especially at large Re and low Ka.

length of the Kapitza instability, are thus dominated by (visco-)capillary forces, and justly designated as "capillary waves". Regarding the earlier cited statements of Chang (1994), we may observe that, although the trend of the capillary wave number in terms of the control parameters (except for frequency) is roughly in agreement with that of the linear cut-off wave number, there is a significant disagreement between the actual values.

Comparing the wave number of the nonlinear capillary waves with the linear cut-off wave number for the *primary flow* is not precisely adequate because the local Reynolds number in the capillary wave region is smaller. However, taking into account a lower Reynolds number, would yield an even lower linear cut-off wave number (dot-dashed line in panel 13b). Meanwhile, the "wiggles" of the solid curves in panels 13c and 13d appear at small wavelengths and large frequencies when the capillary waves directly interact with the back of the next main hump. Each "wiggle" is associated with the addition/subtraction of a capillary hump to/from the train of capillary waves.

We add an observation regarding the linear celerity curves plotted in figure 14b. These curves are composed of a branch that decreases and one that increases with wave number. Thus, the linear behaviour of falling liquid films already allows waves of different wavelength to be matched in celerity. To accommodate considerably disparate wavelengths, the short waves (large wave number) must exit the unstable part of the celerity curve (highlighted by symbols), i.e. transcend the visco-capillary cut-off.

The above conclusions imply that capillary waves on falling liquid films are linearly stable in terms of the Kapitza instability and should attenuate if they were travelling on their own. How is it then possible that they nonetheless attain/maintain a finite amplitude? This could not work if they would behave like capillary waves in the sense of Whitham (1974), the celerity of which depends only on their wave number:

$$\tilde{c} = \left[(\sigma\,\tilde{\alpha}/\rho)\tanh(\tilde{\alpha}\,\tilde{\delta})\right]^{1/2}. \tag{5.1}$$

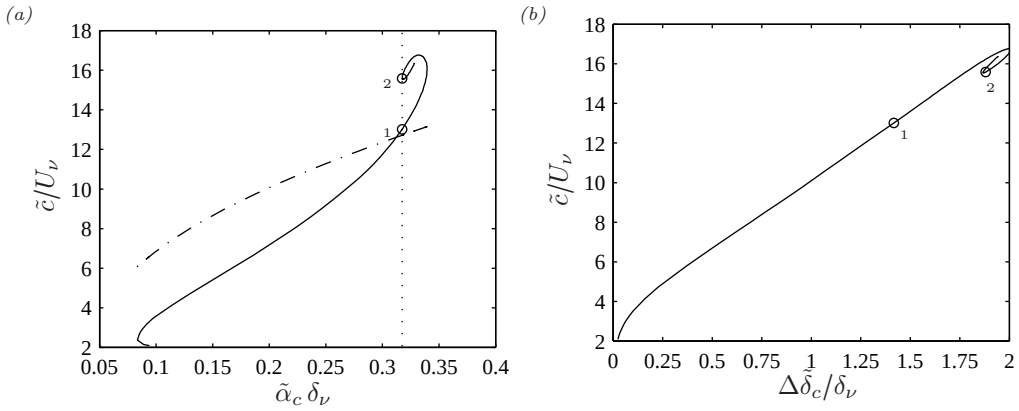

FIGURE 15. Celerity of capillary waves. *(a)* Influence of the wave number. Solid line: nonlinear waves from figure 13a; dot-dashed line: conventional capillary waves in the sense of (Whitham 1974) $\tilde{c} = \left[(\sigma\,\tilde{\alpha}/\rho)\tanh(\tilde{\alpha}\,\tilde{\delta})\right]^{1/2}$; *(b)* influence of the wave amplitude (nonlinear waves), i.e. the height difference between first capillary trough and hump $\Delta\tilde{\delta}$. Here, natural scales are used for non-dimensionalization: $\delta_\nu = (\mu/\rho)^{2/3} g^{-1/3}$ and $U_\nu = (\mu\, g/\rho)^{1/3}$. Contrary to conventional capillary waves, the celerity of capillary waves on falling liquid films depends on their amplitude.

Figure 15a compares this relation (dot-dashed line) with the celerity of the nonlinear capillary waves (solid line), showing a clear discrepancy. Indeed, the nonlinear celerity curve shows that capillary waves of the same wave number may travel at different celerities (e.g. points 1 and 2), which is not compatible with (5.1). This is because their celerity also depends on their amplitude, as shown in panel 15b. More specifically, the capillary wave celerity increases with amplitude. Consequently, considering a capillary wave travelling in front of a main wave hump, it will tend to attenuate due to its linear stability, but this would reduce its celerity, causing the main hump to catch up and compress/speed-up the capillary wave once-again (section 4). We can thus conclude that large wave humps travelling on falling liquid films continuously transfer energy to the precursory capillary ripples for these to maintain a finite amplitude. This is comparable to capillary wakes of objects travelling on liquid surfaces (Raphaël & de Gennes 1996; Moisy & Rabaud 2014).

6. Capillary waves in fully developed wave trains

Once the mechanisms governing the amplitude and celerity of main humps and capillary ripples have settled into an equilibrium, the final wave shape in figure 16 is obtained. Panel 16a represents case 1 and panel 16b case 2, which has a different Reynolds number and wavelength (see table 1). Comparing the two panels, we see that the capillary ripples are significantly altered by changing the wavelength and amplitude of the main humps. We proceed by explaining how this relation is natured based on physical insights from the previous sections. To do so, we again consider the parameter variations performed for figure 13 using the WRIBL model of Ruyer-Quil & Manneville (2000).

We start by varying the Reynolds number Re around the WRIBL simulation of case 1, while maintaining the Kapitza number and wavelength constant. Figure 17 shows wave profiles obtained this way, with Re decreasing from top to bottom. The amplitude of the main humps increases with the Reynolds number due to the mounting relevance of inertia (T_i in equation 3.2) and also increases their celerity. This compresses the precursory capillary waves more and more into a train of increasing curvatures $|\partial_{xx}\delta|$ and decreasing

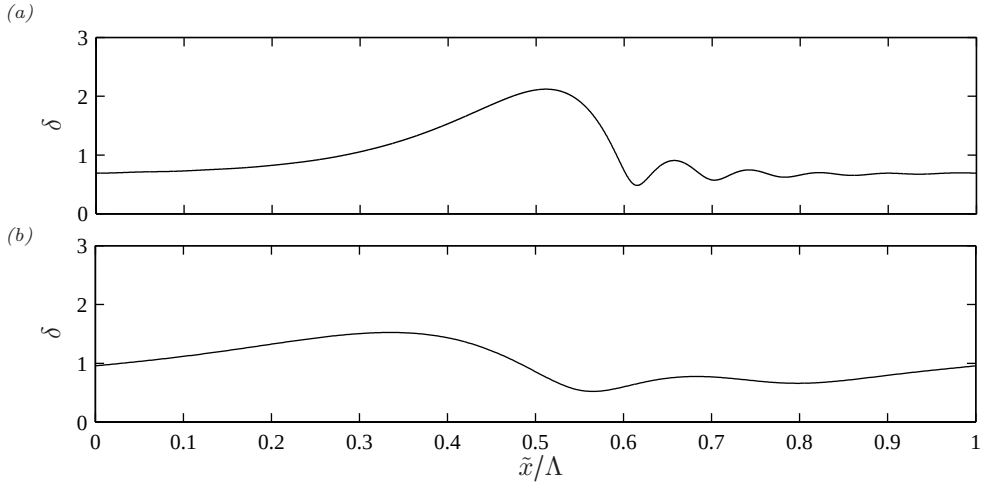

FIGURE 16. Saturated shape of a train of solitary pulses on a falling liquid film, consisting of a main hump and precursory capillary waves, obtained from DNS for cases 1 and 2 in table 1. *(a)* Case 1: Re=15, f=16 Hz; *(b)* case 2: Re=10.7, f=20 Hz. Capillary waves are strongly modified by changing the wavelength and amplitude of the large wave humps.

wavelength, so that capillary and viscous effects (T_p, T_μ and c_p, c_μ in equations 3.2 and 4.1) may arrest the rising inertial contributions and produce a saturated and phase-locked solution. Meanwhile, the number of precursory capillary waves rises with increasing Re, which results from the increasing curvature $\partial_{xx}\delta$ of the first capillary trough. Indeed, the number of capillary waves is fixed by the condition that the last of the *spatially-attenuating* capillary troughs must transition smoothly to the back of the next main hump. Consequently, when the curvature of the first capillary trough is greater, additional spatially-attenuating ripples are needed to sufficiently reduce $\partial_{xx}\delta$.

Figure 18 shows the effect of the large-hump wavelength Λ. Increasing Λ (from the bottom to the top panel) while maintaining the Reynolds and Kapitza numbers constant, increases the linear growth rate of the primary Kapitza instability and, consequently, the amplitude of the large humps. Similarly to the previous figure, this creates increasingly compressed capillary waves of rising number. In contrast to figure 17, the three cases with largest amplitude (panels 18a-18c) develop a flat residual film. This results from the way in which the increase in height of the main humps is sustained in figures 18 and 17, respectively. In figure 18, the Reynolds number and thus the mean film thickness are constant so that the region between two subsequent main humps must increasingly drain in order to sustain their growth. Conversely, in figure 17, the increase in wave height is in part sustained by increasing the mean film thickness, which increases with Re.

Once this flat residual film has formed, the last capillary hump/trough can always smoothly connect to it (as $\partial_x\delta$=0 there) and so the number of capillary ripples ceases to increase. Instead, the length of the capillary wave train is simply shortened. Incidentally, transition from capillary waves interacting with the back of the next main hump to formation of a flat residual film coincides with the "wiggles" in figures 13c and 13d.

Figure 19 shows the effect of reducing the Kapitza number $Ka=\sigma/(\rho\, g^{1/3}\, \nu^{4/3})$ (from top to bottom), which can be achieved e.g. by reducing the surface tension. On the one hand, this directly affects the capillary waves, which increase their curvature magnitude (see $\partial_{xx}\delta$ in bottom right corner of panels) and decrease their wavelength so that capillary-induced growth rate and celerity contributions (T_p, c_p in equations 3.2, 4.1)

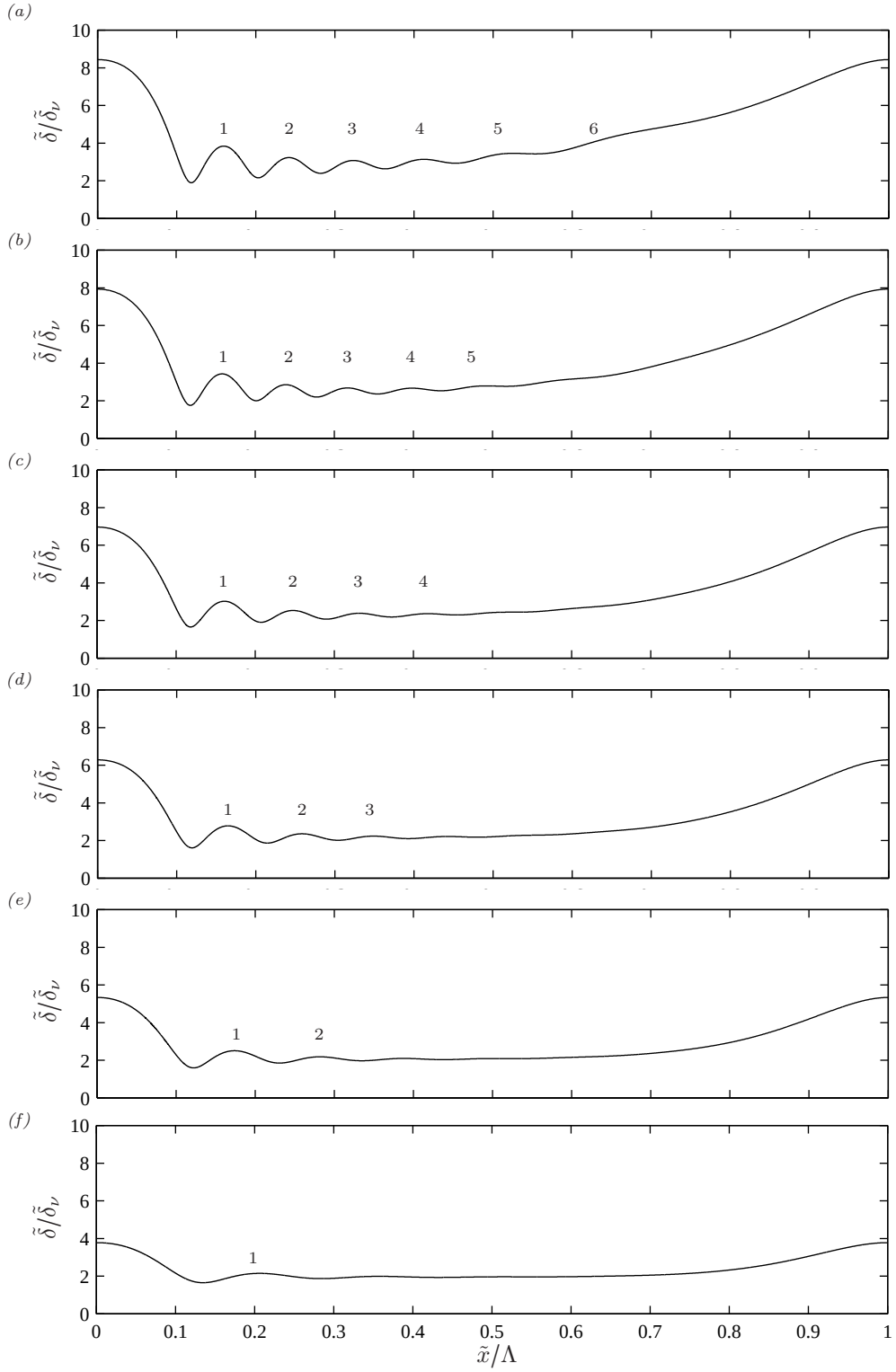

FIGURE 17. Influence of Reynolds number on amplitude, wavelength and number of capillary waves: Ka=509.5; $\Lambda/\tilde{\delta}_\nu$=226, fluid properties according to table 1. Length scale: $\tilde{\delta}_\nu = (\mu/\rho)^{2/3} g^{-1/3}$. *(a)* Re=40, $\tilde{c}$=0.497 m/s; *(b)* Re=30, $\tilde{c}$=0.450 m/s; *(c)* Re=20, $\tilde{c}$=0.384 m/s; *(d)* Re=15 (case 1, table 1), $\tilde{c}$=0.342 m/s; *(e)* Re=10, $\tilde{c}$=0.288 m/s; *(f)* Re=5, $\tilde{c}$=0.202 m/s. Simulations with simplified second-order WRIBL model (Ruyer-Quil & Manneville 2000). Increasing Re increases amplitude of main humps, increasingly compressing capillary waves.

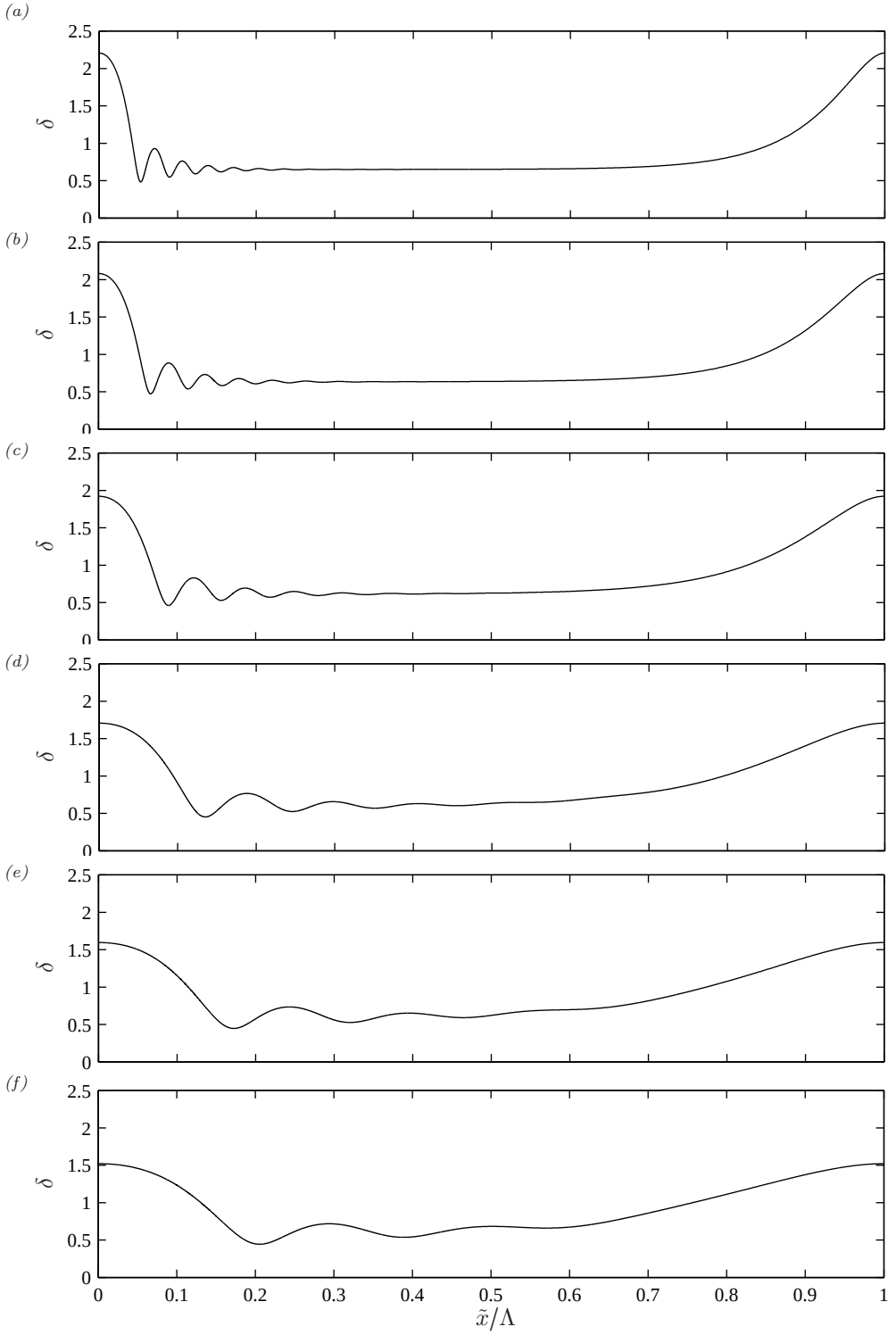

FIGURE 18. Influence of large hump wavelength Λ on amplitude, wavelength and number of capillary waves: Ka=509.5; Re=15, fluid properties according to table 1. *(a)* $\Lambda/\tilde{\delta}_0$=140, $\tilde{c}$=0.438 m/s; *(b)* $\Lambda/\tilde{\delta}_0$=112, $\tilde{c}$=0.410 m/s; *(c)* Λ/δ_0=84, $\tilde{c}$=0.375 m/s; *(d)* $\Lambda/\tilde{\delta}_0$=56, $\tilde{c}$=0.330 m/s; *(e)* $\Lambda/\tilde{\delta}_0$=45, $\tilde{c}$=0.308 m/s; *(f)* $\Lambda/\tilde{\delta}_0$=38, $\tilde{c}$=0.293 m/s. Simulations with simplified second-order WRIBL model (Ruyer-Quil & Manneville 2000). Increasing Λ increases the amplitude of main humps, increasingly compressing capillary waves.

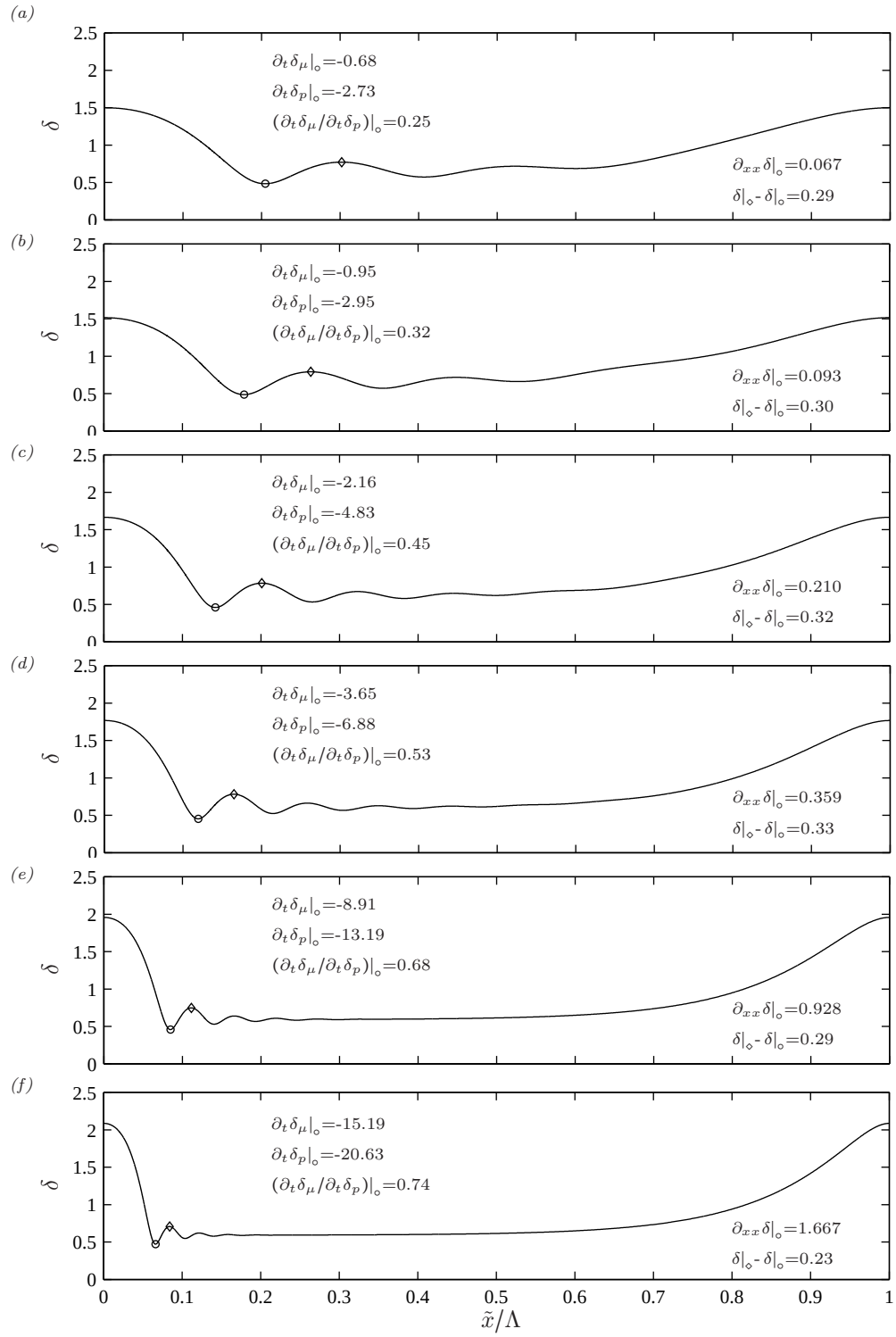

FIGURE 19. Influence of Kapitza number $Ka=\sigma/(\rho\, g^{1/3}\, \nu^{4/3})$ on amplitude, wavelength and number of capillary waves: Re=15; $\Lambda/\tilde{\delta}_0$=63.4, fluid properties (except σ) according to table 1. *(a)* Ka=2000, $\tilde{c}$=0.322 m/s; *(b)* Ka=1400, $\tilde{c}$=0.318 m/s; *(c)* Ka=800, $\tilde{c}$=0.333 m/s; *(d)* Ka=510 (case 1, table 1), $\tilde{c}$=0.343 m/s; *(e)* Ka=200, $\tilde{c}$=0.358 m/s; *(f)* Ka=100, $\tilde{c}$=0.366 m/s. Simulations with simplified second-order WRIBL model (Ruyer-Quil & Manneville 2000). Decreasing Ka increases curvature $\partial_{xx}\delta|_\circ$ by compression of the capillary wave train, until streamwise viscous diffusion becomes strong and dampens the capillary amplitude.

can be maintained in the face of weakening σ, in order to counter inertial contributions (T_i, c_i in equations 3.2, 4.1). On the other hand, reducing surface tension means that the main humps saturate at a greater amplitude and thus travel faster, compressing the capillary wave train even further. This indirect Ka-effect is comparable to figures 17 and 18.

The amplitude of capillary waves in panels 19a to 19d (see $\delta|_\diamond - \delta|_\circ$ in lower right corner) varies very little. Their speed-up mechanism in the face of diminishing Ka mainly consists in reducing their wavelength, which is a capacity already exhibited by the linear celerity curves of figure 14b (therein, capillary waves are situated beyond the symbol-marked unstable branches). Nonetheless, when the capillary wavelength becomes very small (panels 19e and 19f), the capillary amplitude starts to decrease noticeably. This is due to streamwise viscous diffusion (T_μ, c_μ in equations 3.2, 4.1), which increases its relative importance as Ka diminishes and streamwise velocity gradients between capillary troughs and humps become strong. In this low Ka limit, the capillary waves still significantly increase their curvature $|\partial_{xx}\delta|$ with decreasing Ka but they do this while reducing *both* their wavelength *and* their amplitude. This is in agreement with Ruyer-Quil & Manneville (2000) (see figure 5 there), who observed that "switching on" streamwise viscous diffusion in their WRIBL model reduces the capillary amplitude and wavelength.

To explain this intricate effect, we extract the growth rate contribution of streamwise viscous diffusion $\partial_t\delta_\mu$ from the WRIBL model, i.e. equation (41) in Ruyer-Quil & Manneville (2000). This is possible in the case of travelling waves, where we may employ $q = q_{\mathrm{MF}} + c\,\delta$ to express the flow rate in terms of the film thickness and the moving-frame-flow-rate $q_{\mathrm{MF}} = q_0 - c\,\bar{\delta} < 0$:

$$\partial_t\delta_\mu = \frac{1}{Re}\left[4\frac{q_{\mathrm{MF}}}{c\,\delta^2} - \frac{1}{2\,\delta}\right](\partial_x\delta)^2 - \frac{1}{Re}\left[6\frac{q_{\mathrm{MF}}}{c\,\delta} + \frac{3}{2}\right]\partial_{xx}\delta, \tag{6.1a}$$

whereas the capillary contribution $\partial_t\delta_p = -\partial_x T_p$ is given by:

$$\partial_t\delta_p = \frac{5}{2\,c}\frac{1}{\mathrm{Bo}\,Re}\delta\partial_{xxx}\delta. \tag{6.1b}$$

These two quantities as well as $\partial_t\delta_\mu/\partial_t\delta_p$ are quantified in panels 19a-19f, confirming that the relative importance of $\partial_t\delta_\mu$ rises significantly with decreasing Ka.

Inspecting (6.1a), we see that the RHS consists of two terms, one that is proportional to $(\partial_x\delta)^2$ and always negative, and another that is proportional to $\partial_{xx}\delta$. The second term is active at the capillary humps and troughs, while the first is active in the flanks separating these extrema and does not differentiate between ascending ($\partial_x\delta > 0$) and descending ($\partial_x\delta < 0$) flanks. Both terms react differently to changes in the wavelength of the capillary waves and this explains how the latter are modified between panels 19e and 19f. We have established that the capillary wave train needs to be compressed from panel 19e to 19f to compensate for the loss in surface tension. This compression increases the curvature magnitude at the extrema and thus the magnitude of $\partial_t\delta_\mu$ there. However, if the compression were realized at constant amplitude, the increase in slope of the capillary flanks would be too great, producing a too negative $\partial_t\delta_\mu$ there. Consequently, this slope is reduced by decreasing the height difference between capillary humps and troughs.

In summary, when streamwise viscous diffusion becomes a coequal stabilizing mechanism (at low Ka), capillary waves are, as usual, compressed, producing large curvature magnitudes at the capillary extrema. But, this compression is done at diminishing amplitude in order to reduce the slope of the capillary flanks compared to a constant-amplitude compression. Decreasing the Kapitza number beyond its value in figure 19f, further re-

duces the capillary wave amplitude, yet an increasingly curved capillary trough always remains, until the limiting case of a shock (where $\partial_{xx}\delta$ is infinite) is reached at σ=0.

7. Conclusion

The typical shape of a fully-developed train of solitary pulses travelling on a vertically falling liquid film is represented in figures 1 and 16. It consists of a large-amplitude asymmetrical (tear-shaped) main hump of long wavelength, which is preceded by a number of small-amplitude small-wavelength ripples, travelling in phase lock. We have investigated these precursory ripples based on direct numerical simulations (section 3 to 5) as well as low-dimensional models (sections 2 and 6) in order to answer the following questions.

(i) How do precursory ripples form on wavy falling liquid films? Precursory ripples evolve from single-peaked wave solutions once the amplitude of the main hump becomes large and its leading front sufficiently steepens. The first ripple-trough does not emerge from the global trough of the single-peaked wave but forms within the leading wave front (figure 6), close to the locus where the free-surface curvature is positively maximal (figure 7). There, the inertia-induced growth rate contribution ($-\partial_x T_i$ in (3.2b) and panel 10f) is dominantly negative, causing a new global trough to form. Thereby, occurrence of a curvature maximum within the leading wave front is a property already exhibited by kinematic waves (figure 2). Growth of the first ripple-trough (figure 6) produces a local negative curvature maximum slightly downstream (figure 7), which generates a corresponding ripple-*hump* and so on and so forth (figure 8) until a train of ripples covers the residual film separating subsequent large humps (figure 16).

(ii) How can capillary waves travel at the same celerity as the main humps? Linear stability analysis (figure 14b) already shows that waves of disparate wavelengths can travel at the same speed on falling liquid films. Physically, it is the effect of surface tension forces (as well as streamwise viscous diffusion) that allows large humps and precursory ripples to match their respective celerities. The capillary-induced contribution to the nonlinear wave celerity (c_p in (4.1) and figure 21) is negative at the main hump, thus slowing it down, and positive at the ripple trough, thus speeding it up. The magnitude of this term in relation to the opposite-sign inertial contribution (c_i in (4.1) and figure 21) rises when the main hump and ripple trough are increasingly compressed (figures 11 and 12), as the initially fast-travelling main wave catches up with the initially slow-travelling precursory ripple, until phase lock is eventually achieved.

(iii) Why are the precursory ripples designated as "capillary waves"? Precursory ripples are justly designated as "capillary waves", because their wavelength is systematically shorter than the visco-capillary cut-off wavelength of the Kapitza instability (figure 13). They are thus stable and would attenuate if they were travelling on their own. That they nonetheless reach a finite amplitude results from a nonlinear effect, namely that their celerity decreases with amplitude (figure 15b). This tends to slow-down decaying capillary waves relative to the pursuing main hump and causes the latter to re-approach and re-compress the capillary waves into a faster-travelling shape (see *(ii)* above). Capillary waves are thus sustained at finite amplitude by the main hump, which constantly transfers energy to compensate dissipation. This is similar to capillary wakes around objects travelling on a liquid surface (Raphaël & de Gennes 1996; Moisy & Rabaud 2014).

(iv) Under what conditions do many/few strongly/weekly-pronounced capillary waves occur? The number and degree of compression of capillary waves is governed by the amplitude of the main wave humps as well as the Kapitza number. Large-amplitude main humps travel fast and strongly compress the capillary waves in order for these to speed-up sufficiently (figure 18). This also affects the number of capillary waves, because the more

pronounced the first capillary wave becomes, the more (spatially attenuating) capillary waves are needed to allow a smooth transition to the back of the next main hump. This is shown in figures 17, 18, and 19, where the main hump amplitude was increased trough increasing the Reynolds-number/main-wavelength and decreasing the Kapitza number, respectively. There is also a strong direct Kapitza number effect. Decreasing Ka, significantly increases the curvature magnitude at the capillary trough (figure 19) in order for capillary growth rate and celerity contributions to remain sufficiently strong to compensate inertial contributions in the face of diminishing surface tension. Then, once the Kapitza number is very small, streamwise viscous diffusion becomes increasingly important. This effect tends to decrease the amplitude of capillary waves while their curvature magnitude is increased, until the limiting case of a shock is reached at σ=0.

Acknowledgements

The author thanks Manfred Zeller, Cameron Tropea, Michael Dreyer, and Jeff Porter for their questions, which were the motivation behind this work. Also, financial support from CNRS institute INSIS is gratefully acknowledged.

8. Appendix

Figures 20 and 21 show results of a simulation almost identical to case 1 in table 1 and are to be compared with figures 6 and 11. The difference between the two simulations is that a greater initial Reynolds number is imposed in figures 20 and 21. This increases the relevance of inertia, amplifying the sequence of events producing the first capillary trough. Figure 21 shows that the capillary celerity contribution c_p (see equation 4.1) speeds up the capillary trough and slows down the hump, while the inertial contribution c_i slows down the trough and speeds up the hump. Figure 22 compares data obtained by different numerical simulation methods throughout this manuscript (DNS, simulations based on (2.2), and WRIBL simulations) with experimental data of Dietze *et al.* (2009). The coefficients of the second-order Benney equation (2.10) used in section 2 are:

$$\begin{aligned} &D(\delta) = 7\delta^3 + \frac{381}{35}Re^2\delta^9,\ E(\delta) = 3\delta^4 + \frac{12}{7}Re^2\delta^{10},\ F(\delta) = \frac{10}{7}\frac{Re}{\mathrm{Bo}}\delta^7, \\ &G(\delta) = 12\frac{Re}{\mathrm{Bo}}\delta^6,\ H(\delta) = \frac{36}{5}\frac{Re}{\mathrm{Bo}}\delta^6,\ I(\delta) = \frac{72}{5}\frac{Re}{\mathrm{Bo}}\delta^5. \end{aligned} \tag{8.1}$$

REFERENCES

Alekseenko, S. V., Nakoryakov, V. E. & Pokusaev, B. G. 1994 *Wave Flow of Liquid Films*. Begell House.

Benney, D. J. 1966 Long waves on liquid films. *Journal of Mathematics and Physics* **45**, 150–155.

Brooke Benjamin, T. 1957 Wave formation in laminar flow down an inclined plane. *Journal of Fluid Mechanics* **2**, 554–574.

Chang, H. C. 1994 Wave evolution on a falling film. *Annual Review of Fluid Mechanics* **26**, 103–136.

Chang, H. C. & Demekhin, E. A. 2002 *Complex Wave Dynamics on thin Films. Studies in Interface Science* 14. Amsterdam: Elsevier.

Chang, H. C., Demekhin, E. A., Kalaidin, E. & Ye, Y. 1996 Coarsening dynamics of falling-film solitary waves. *Physical Review E* **54** (2), 1467–1477.

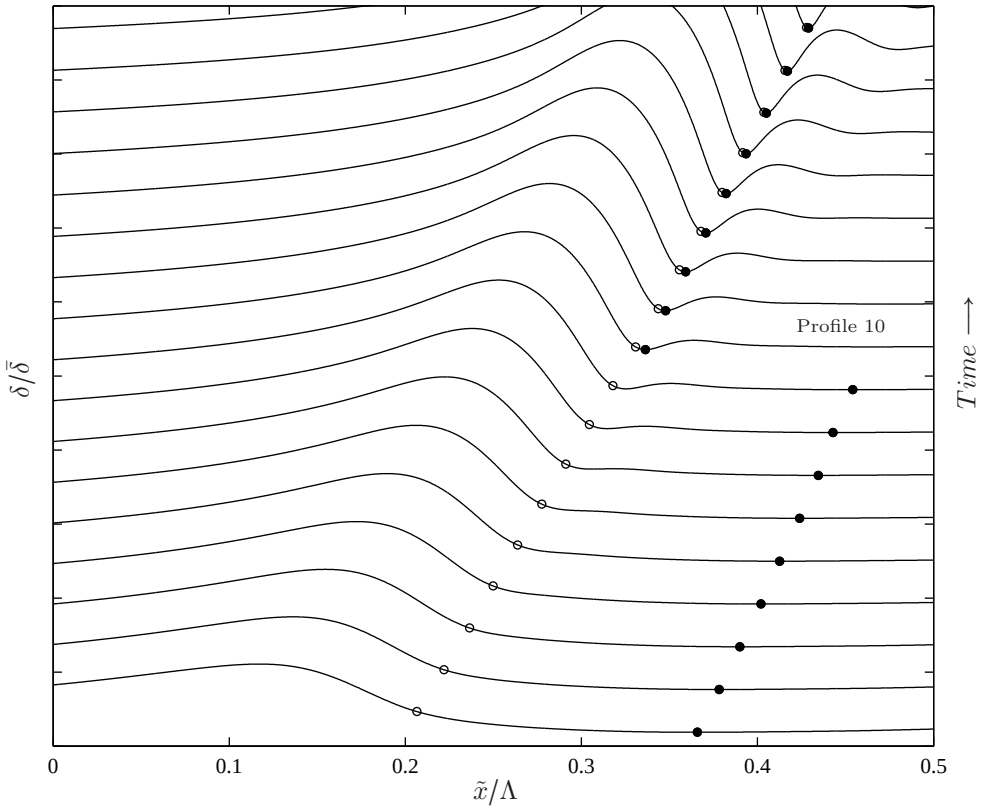

FIGURE 20. Direct numerical simulation corresponding almost exactly to the one presented in figure 6: $\bar{\tilde{\delta}}$=302 μm, Re^{∞}=15, $\tilde{f}^{\infty}$=16 Hz, Ka=509.5. The only difference here is that a greater initial Reynolds number is imposed (for the tenth profile, Re=38 compared to Re=13.5 in figure 6), producing a more pronounced sequence of the events surrounding the inception of the first capillary wave in figure 6. This Reynolds number effect confirms our finding that an inertia-based mechanism produces the first capillary trough. The timespan represented is $t = \tilde{t}/\tau \in [1 : 0.05 : 1.8]$ (time scale: $\tau=(H^3\rho/\sigma)^{1/2}$, with H=1.5 mm denoting the height of the DNS domain). Profiles are each represented over a film thickness interval of $\delta/\bar{\delta} \in [0.4, 2.4]$.

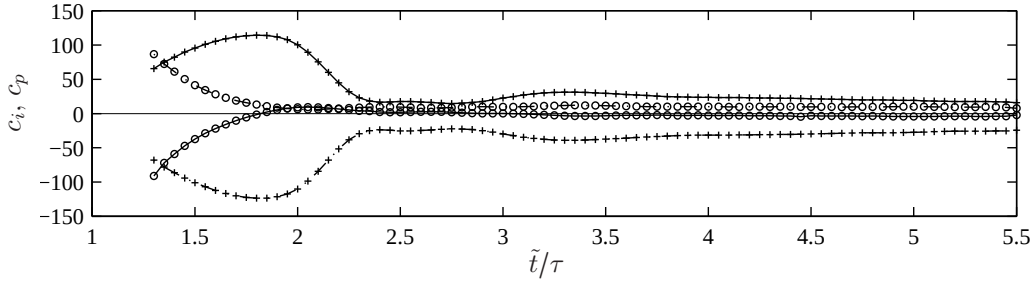

FIGURE 21. Time evolution (τ as in figure 20) of wave celerity contributions in (4.1) evaluated respectively at the main hump (plus signs) and capillary trough (open circles) in figure 20. Solid lines: contribution of inertia c_i; Dot-dashed lines: contribution of pressure c_p.

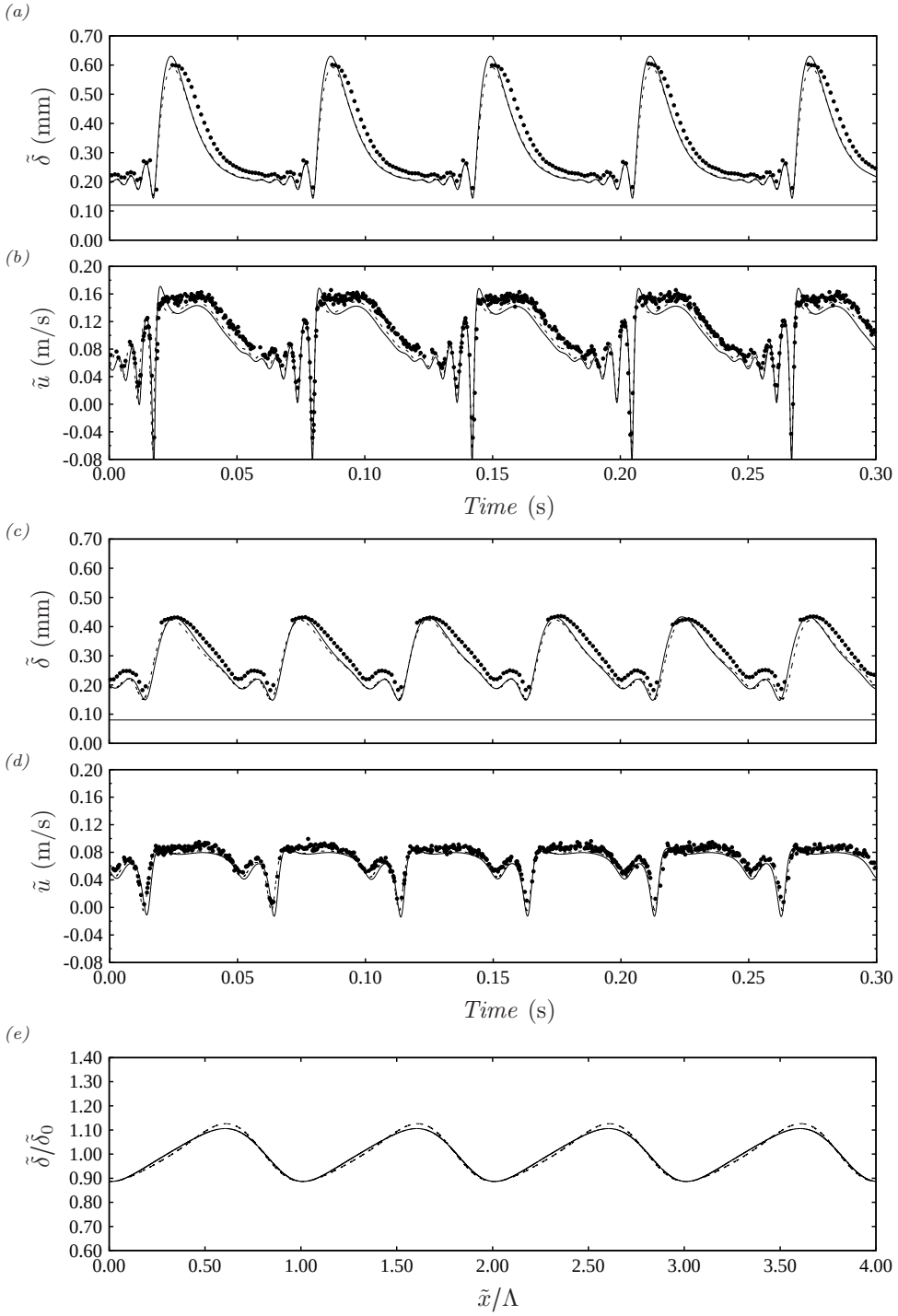

FIGURE 22. Validation of model simulations (based on equation (2.2) and the WRIBL model of Ruyer-Quil & Manneville (2000), respectively) and DNS with experimental data of Dietze *et al.* (2009). *(a-d)* Film thickness (*a,c*) and streamwise velocity (*b,d*) time traces from experiment (filled circles), DNS (solid lines), and WRIBL simulations (dashed lines), respectively (velocity data are evaluated at $y = 120$ μm (panel *b*) and $y = 80$ μm (panel *d*), respectively): cases 1 (*a-b*) and 2 (*b-d*) from table 1. *(e)* Spatial film thickness profile obtained from the WRIBL model (solid lines) and equation (2.2) (dashed lines), respectively: conditions according to figure 4.

Chang, H. C., Demekhin, E. A. & Kopelevich, D. I. 1993 Nonlinear evolution of waves on a vertically falling film. *Journal of Fluid Mechanics* **250**, 433–480.

Craster, R. V. & Matar, O. K. 2009 Dynamics and stability of thin liquid films. *Reviews of Modern Physics* **81**, 1131–1198.

Demekhin, E. A., Kalaidin, E. N., Kalliadasis, S. & Vlaskin, S. Yu. 2007*a* Three-dimensional localized coherent structures of surface turbulence. I. scenarios of two-dimensional-three-dimensional transition. *Physics of Fluids* **19** (114103), 114103.

Demekhin, E. A., Kalaidin, E. N., Kalliadasis, S. & Vlaskin, S. Yu. 2007*b* Three-dimensional localized coherent structures of surface turbulence. II. solitons. *Physics of Fluids* **19** (114103), 114104.

Demekhin, E. A., Kalaidin, E. N., Kalliadasis, S. & Vlaskin, S. Yu. 2010 Three-dimensional localized coherent structures of surface turbulence: Model validation with experiments and further computations. *Phys. Rev. E* **82** (114103), 036322.

Dietze, G. F. 2010 Flow Separation in Falling Liquid Films. PhD thesis, RWTH Aachen University. ISBN 978-3-86844-259-5.

Dietze, G. F., Al-Sibai, F. & Kneer, R. 2009 Experimental study of flow separation in laminar falling liquid films. *Journal of Fluid Mechanics* **637**, 73–104.

Dietze, G. F., Leefken, A. & Kneer, R. 2008 Investigation of the backflow phenomenon in falling liquid films. *Journal of Fluid Mechanics* **595**, 435–459.

Dietze, G. F., Rohlfs, W., Nährich, K., Kneer, R. & Scheid, B. 2014 Three-dimensional flow structures in laminar falling liquid films. *Journal of Fluid Mechanics* **743**, 75–123.

Doedel, E. J. 2008 AUTO07p: Continuation and bifurcation software for ordinary differential equations. *Montreal Concordia University* .

Doro, E. O. & Aidun, C. 2013 Interfacial waves and the dynamics of backflow in falling liquid films. *Journal of Fluid Mechanics* **726**, 261–284.

Floryan, J. M., Davis, S. H. & Kelly, R. E. 1987 Instabilities of a liquid film flowing down a slightly inclined plane. *Physics of Fluids* **30** (4), 983–989.

Gao, D., Morley, N. B. & Dhir, V. 2003 Numerical simulation of wavy falling film flow using VOF method. *Journal of Computational Physics* **192**, 624–642.

Gjevik, B. 1970 Occurence of finite-amplitude surface waves on falling liquid films. *The Physics od Fluids* **13** (8), 1918–1925.

Joo, S. W. & Davis, S. H. 1992 Instabilities of three-dimensional viscous falling films. *Journal of Fluid Mechanics* **242**, 529–547.

Kalliadasis, S., Ruyer-Quil, C., Scheid, B. & Velarde, M. G. 2012 *Falling Liquid Films*, Applied Mathematical Sciences, vol. 176. Springer.

Kapitza, P. L. 1948 Wave flow of thin layer of viscous fluid (in Russian). *Zhurn. Eksper. Teor. Fiz.* **18** (1), 3–28.

Kofman, N., Mergui, S. & Ruyer-Qui, C. 2014 Three-dimensional instabilities of quasi-solitary waves in a falling liquid film. *Journal of Fluid Mechanics* **757**, 854–887.

Lel, V.V., Al-Sibai, F., Leefken, A. & Renz, U. 2005 Local thickness and wave velocity measurement of wavy films with a chromatic confocal imaging method and a fluorescence intensity technique. *Experiments in Fluids* **39** (5), 856–864.

Lin, S. P. 1974 Finite amplitude side-band stability of a viscous film. *Journal of Fluid Mechanics* **63**, 417–429.

Liu, J. & Gollub, J. P. 1994 Solitary wave dynamics of film flows. *Physics of Fluids* **6** (5), 1702–1712.

Liu, J., Paul, J.D. & Gollub, J. P. 1993 Measurements of the primary instabilities of film flows. *Journal of Fluid Mechanics* **250**, 69–101.

Malamataris, N. A. & Balakotaiah, V. 2008 Flow structure underneath the large amplitude waves of a vertically falling film. *AIChE Journal* **54** (7), 1725–1740.

Malamataris, N. A., Vlachogiannis, M. & Bontozoglou, V. 2002 Solitary waves on inclined films: Flow structure and binary interactions. *Physics of Fluids* **14** (3), 1082–1094.

Miyara, A. 1999 Numerical analysis on flow dynamics and heat transfer of falling liquid films with interfacial waves. *Heat and Mass Transfer* **35**, 298–306.

Moisy, F. & Rabaud, M. 2014 Mach-like capillary-gravity wakes. *Physical Review E* **90**, 023009.

Nosoko, T. & Miyara, A. 2004 The evolution and subsequent dynamics of waves on a vertically falling liquid film. *Physics of Fluids* **16** (4), 1118–1126.

Oron, A., Davis, S. H. & Bankoff, S. G. 1997 Long-scale evolution of thin liquid films. *Reviews of Modern Physics* **69** (3), 931–980.

Park, C. D. & Nosoko, T. 2003 Three-dimensional wave dynamics on a falling film and associated mass transfer. *AIChE Journal* **49** (11), 2715–2727.

Popinet, S. 2009 An accurate adaptive solver for surface-tension-driven interfacial flows. *J. Comput. Phys.* **228**, 5838–5866.

Pradas, M., Kalliadasis, S., Nguyen, P.-K. & Bontozoglou, V. 2013 Bound-state formation in interfacial turbulence: direct numerical simulations and theory. *Journal of Fluid Mechanics* **716**, R2.

Pradas, M., Tseluiko, D. & Kalliadasis, S. 2011 Rigorous coherent-structure theory for falling liquid films: Viscous dispersion effects on bound-state formation and self-organization. *Physics of Fluids* **23**, 044104.

Pumir, A., Manneville, P. & Pomeau, Y. 1983 On solitary waves running down an inclined plane. *J. Fluid Mech.* **135**, 27–50.

Ramaswamy, B., Chippada, S. & Joo, S. W. 1996 A full-scale numerical study of interfacial instabilities in thin-film flows. *Journal of Fluid Mechanics* **325**, 163–194.

Raphaël, E. & de Gennes, P.-G. 1996 Capillary gravity waves caused by a moving disturbance: Wave resistance. *Physical Review E* **53**, 3448.

Rohlfs, W & Scheid, B. 2015 Phase diagram for the onset of circulating waves and flow reversal in inclined falling films. *Journal of Fluid Mechanics* **763**, 322–351.

Ruyer-Quil, C. & Manneville, P. 1998 Modeling film flows down inclined planes. *European Physical Journal B* **6** (2), 277–292.

Ruyer-Quil, C. & Manneville, P. 2000 Improved modeling of flows down inclined planes. *European Physical Journal B* **15** (2), 357–369.

Salamon, T. R., Armstrong, R. C. & Brown, R. A. 1994 Traveling waves on vertical films: Numerical analysis using the finite element method. *Physics of Fluids* **6**, 2202–2220.

Shkadov, V. Ya. 1967 Wave flow regimes of a thin layer of viscous fluid subject to gravity. *Fluid Dynamics* **2** (1), 29–34.

Tihon, J., Serifi, K., Argyriadi, K. & Bontozoglou, V. 2006 Solitary waves on inclined films: their characteristics and the effects on wall shear stress. *Experiments in Fluids* **41**, 79–89.

Trifonov, Y. Y. 2008 Wavy film flow down a vertical plate: Comparisons between the results of integral approaches and full-scale computations. *Journal of Engineering Thermophysics* **17** (1), 30–52.

Whitham, G. B. 1974 *Linear and Nonlinear Waves*. New York: John Wiley & Sons.

Yih, C. S. 1963 Stability of liquid flow down an inclined plane. *The Physics of Fluids* **6** (3), 321–334.